International Communications in Heat and Mass Transfer 163 (2025) 108738

Contents lists available at ScienceDirect

International Communications in Heat and Mass Transfer

journal homepage: www.elsevier.com/locate/ichmt

Oil-CO_2 phase behavior in nanoporous media: A lattice Boltzmann study

Han Wang [a], Qinjun Kang [b], Wendong Wang [c,d], Wu He [a], Yuxuan Xia [a], Jianchao Cai [a,*]

[a] State Key Laboratory of Petroleum Resources and Engineering, China University of Petroleum, Beijing 102249, China
[b] Earth and Environmental Sciences Division, Los Alamos National Laboratory, Los Alamos, NM 87545, USA
[c] National Key Laboratory of Deep Oil and Gas, China University of Petroleum (East China), Qingdao 266580, China
[d] School of Petroleum Engineering, China University of Petroleum (East China), Qingdao 266580, China

ARTICLE INFO

Keywords:
Oil-CO_2 phase behavior
Immiscible diffusion
Competitive adsorption
Nanoporous media
Lattice Boltzmann method

ABSTRACT

The complex phase behaviors of oil-CO_2 immiscible diffusion and oil swelling in shale nanoscale space under the influence of competitive adsorption caused by fluid-solid interaction force are still unclear, which is significantly important for shale oil recovery and carbon sequestration. In this paper, a multi-relaxation-time lattice Boltzmann method integrating the two-phase two-component three-distribution Shan-Chen flow model and mass transfer model is established to simulate the CO_2 diffusion through immiscible phase interfaces, oil-dissolved CO_2 competitive adsorption on the mineral surfaces, and oil swelling in nanoporous media. The proposed model is verified by the microfluidic experiment to successfully capture the diffusion and swelling. Then, the effects of equilibrium dissolution concentration and competitive adsorption on CO_2 diffusion/dissolution and oil swelling are studied. The results show that as the equilibrium dissolution concentration increases, the dissolution rate of CO_2 is accelerated, resulting in the increase of oil swelling volume and the dissolved CO_2 adsorption concentration. The mass of CO_2 diffusing into the oil phase increases with CO_2 adsorption capacity, but the oil swelling volume decreases because of the increased CO_2 adsorption on mineral surfaces.

1. Introduction

Shale reservoirs exhibit characteristics such as nanoscale pore structures (2–200 nm), low porosity, low permeability, multiple mineral compositions, and diverse fluid types (hydrocarbons, CO_2, and water) [1]. Unlike conventional scales, the behavior of multiphase and multicomponent fluids in nanoscale space is significantly affected by molecular interactions, making them more complex and challenging to characterize [2–4]. The complicated physical and chemical behaviors of shale fluids include oil/gas single-phase flow considering nanoscale effects (e.g., slip, diffusion, heterogeneous fluid properties) [5,6]. Additionally, due to the infiltration of primary water and fracturing fluid into the pore space via capillary force, the single-phase flow evolves into oil-water and gas-water two-phase flows with additional consideration of liquid-liquid interfacial slip [7–9]. As shale oil is extracted, the reservoir pressure gradually drops below the bubble point pressure, causing the low-molecular-weight hydrocarbon to precipitate and form an oil-gas two-phase flow [10,11]. Shale reservoirs are generally developed using CO_2 injection, and the injected CO_2 can diffuse into the oil phase through the immiscible/miscible oil-CO_2 interface under varying reservoir pressure and temperature conditions [12–14]. Meanwhile, due to the great adsorption of CO_2 on mineral surfaces, CO_2 can competitively adsorb and replace the adsorbed oil [15,16]. When the adsorbed CO_2 reaches saturation, CO_2 can be miscible with the bulk oil to cause the oil swelling and viscosity reduction, which ultimately affects oil-CO_2 immiscible/miscible flow behaviors [17]. However, compared to oil/gas/water multiphase flows, accurately characterizing the behaviors of oil-CO_2 phase change, diffusion, competitive adsorption, and oil swelling still confronts significant challenges, which is not only of great significance for enhancing shale oil recovery but also friendly to the green environment through CO_2 geological sequestration.

Under different pressure and temperature conditions, CO_2 and underground fluids phases exhibit different and unique physical and chemical behaviors [18–22]. With the pressure and temperature reaching 7.38 MPa and 31.2 °C, CO_2 transitions from a gaseous state to a supercritical state, demonstrating the physical properties of increasing density, near-zero surface tension, and lower viscosity [23–25]. Supercritical CO_2 also exhibits excellent injection performance and solubility, effectively supplementing formation energy [26]. When the reservoir pressure reaches the minimum miscibility pressure (MMP), CO_2 and shale oil lose their distinct phase interface characteristics, resulting in zero interfacial tension. Over sufficient time, CO_2 and oil can be

* Corresponding author.
E-mail address: caijc@cup.edu.cn (J. Cai).

https://doi.org/10.1016/j.icheatmasstransfer.2025.108738

Available online 24 February 2025

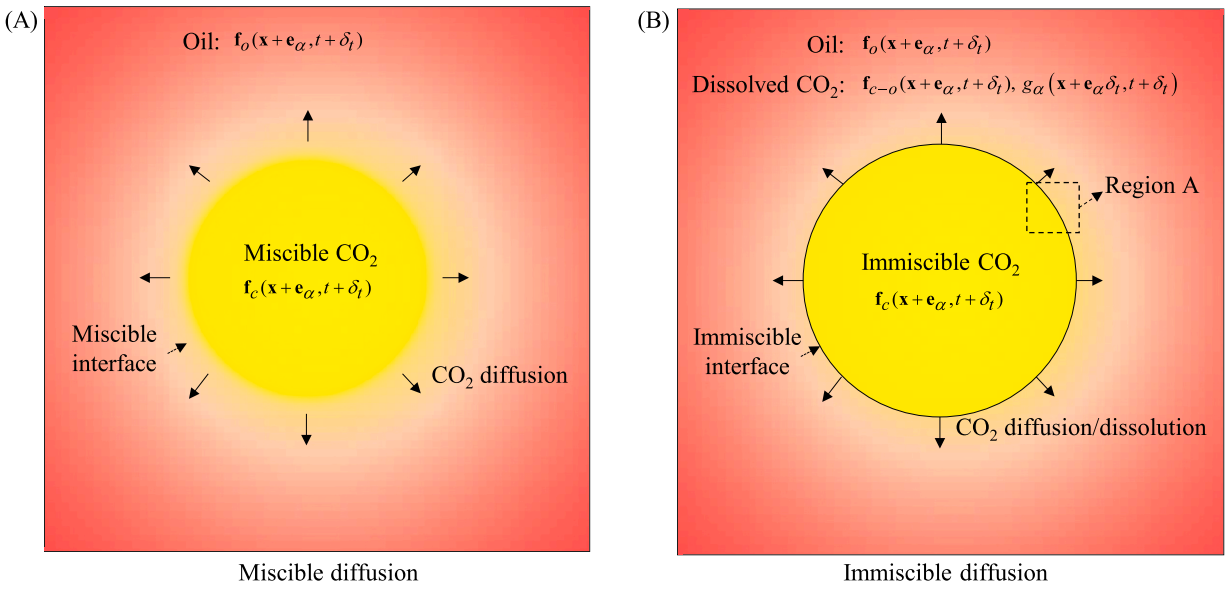

Fig. 1. The schematic diagram of miscible diffusion and immiscible diffusion of CO_2 droplets into the oil phase. (A) Miscible diffusion. Both oil and CO_2 phases are characterized by a two-distribution D2Q9 LB flow model; (B) Immiscible diffusion. The oil, dissolved CO_2, and immiscible CO_2 phases are characterized by a three-distribution D2Q9 LB flow model. The dissolved CO_2 is also characterized by a D2Q5 LB mass transfer model. The gradual change in colour from yellow to red in the oil phase indicates the decrease of dissolved CO_2 concentration. Yellow: CO_2, Red: oil. (For interpretation of the references to colour in this figure legend, the reader is referred to the web version of this article.)

completely miscible, further enhancing recovery. Li et al., 2017 indicated that the injection pressure should be higher than the MMP to achieve higher shale oil recovery [24]. However, the MMP between shale oil and CO_2 can be up to 23 MPa [27,28], and maintaining the complete miscible pressure during CO_2 huff-n-puff and production processes is challenging [29]. Even if the MMP cannot be reached to form a complete miscible phase under reservoir conditions, CO_2 can still diffuse into oil through the interfacial region until the dissolved CO_2 concentration in the oil phase reaches the equilibrium dissolution concentration, and exert the oil swelling and viscosity reduction. The diffusion process of CO_2 through an immiscible interface is elucidated in detail in Fig. 1B. Yu et al., 2021 investigated the impact of injection pressure on shale oil extraction using CO_2 in an immiscible state. The results indicated that the higher injection pressures enhance CO_2 solubility in the oil phase and accelerate mass transfer effect [30]. On the contrary, as the reservoir pressure decreases, miscible CO_2 in the oil phase tends to precipitate out to form gas bubbles due to the decreasing solubility.

The efficiency of injected CO_2 relies on the development of the phase behavior effect between oil and CO_2, which depends on the contact time, diffusion path, diffusion rate, and solubility [31,32]. Additionally, in the nanoscale space, it is further affected by the oil-CO_2 competitive adsorption on mineral surfaces, which is dictated by their differing affinities for mineral surfaces [17]. Zhang et al., 2021 investigated the influence of CO_2 mass content in shale oil phase on the viscosity reduction and the oil flow. The results revealed that when the CO_2 mass percentage is less than about 19 %, approximately 93 % of the CO_2 is adsorbed on mineral surfaces, while about 7 % of CO_2 in the bulk oil has a negligible impact on reducing viscosity and enhancing flow [33]. Moh et al., 2022 investigated the CO_2 diffusion into the nanopore-saturated oil through molecular simulation, demonstrating that CO_2 diffuses along the solid surface into the pores due to CO_2 adsorption [34]. Therefore, under varying pressure and temperature conditions, oil and CO_2 can undergo complex processes of both miscible and immiscible diffusion. Additionally, the fluid-solid interaction force in the nanoscale space cannot be ignored, causing the oil-CO_2 competitive adsorption behaviors. Understanding the complex oil-CO_2 phase behaviors is crucial for enhancing shale oil recovery and CO_2 geological storage. These behaviors are challenging to elucidate through experiments or conventional numerical simulations [35,36]. Molecular simulations, while powerful, are constrained by computational resources and typically focus on single nanopores [37].

Alternatively, the microscopic interaction mechanisms can be effectively elucidated through pore-scale simulation methods, including both indirect and direct simulation methods [38–40]. The indirect simulation method generally refers to pore network models, widely applied for single-phase flow, immiscible multiphase flow, and diffusion behaviors [41]. However, they may not fully capture interface characteristics and competitive adsorption phenomena in oil-CO_2 miscible/immiscible systems. Moreover, due to the simplified pore-throat structures, the calculation results may lack a certain accuracy. For the direct simulation methods, Zhu et al., 2024 presented a CFD-based workflow to simulate CO_2-oil miscible flooding in tight porous media, and discussed the effects of Péclet number, microfracture, and adsorption/desorption on CO_2 storage and oil production. However, this method cannot be applied to the diffusion of oil-CO_2 immiscible-phase systems, and the dynamic processes of adsorption/desorption are not intuitive [42]. The lattice Boltzmann method (LBM) is a popular direct simulation method, which is widely used to model the complex physical and chemical behaviors of multicomponent and multiphase fluids [43–46]. The multiphase LBM mainly includes colour-gradient model [47], pseudopotential model [48] and free-energy model [49], in which the pseudopotential model proposed by Shan-Chen stands out as the most popular due to its simplicity and versatility [50]. Compared with the Bhatnagar–Gross–Krook (BGK) collision operator used in the original Shan-Chen model, the multi-relaxation-time (MRT) model has gained widespread adoption in recent years due to the advantages of numerical stability [51,52]. LBM can effectively capture the CO_2 diffusion characteristics and competitive adsorption characteristics [15,53,54]. Wang et al., 2022 developed a lattice Boltzmann (LB) model to study oil-CO_2 diffusion and competitive adsorption behaviors in shale porous media. However, their model is limited to pressure conditions above the MMP [17]. When the formation pressure is smaller than MMP, CO_2 diffuses into the oil phase through the immiscible oil-CO_2 interface. Currently, LBM is generally applied to simulate the diffusion/dissolution between CO_2/methane and water phase to explore mineral dissolution and

Table 1
Comparison of the proposed methodology and previous work.

Property	Previous work [17]	Proposed methodology
Number of phases	one	two
Governing equations of flow	two-distribution function	three-distribution function
Governing equations of diffusion	\	1
Physical problem	Oil-CO_2 miscible behavior	Oil-CO_2 immiscible behavior

hydrate dissolution [55–57], however, this method is limited to conventional scales and does not account for the fluid-solid interaction forces in nanoscale space. Moreover, the forms of dissolved CO_2 in oil and water are fundamentally different. In the water phase, CO_2 exhibits low solubility, mainly exists in the form of ions, exerting a weak impact on the viscosity and density of water. However, a large amount of CO_2 can be dissolved in oil as the pressure increases, as a result, CO_2 is miscible with the oil phase in the form of an important component. The dissolved CO_2 can substantially impact the viscosity, density and swelling factor of the oil phase [33]. The current LB models are inadequate for the complicated oil-CO_2 phase behaviors in nanoporous media with reservoir pressure below MMP.

Therefore, in this work, the LBM coupling the multiphase multicomponent flow model with a mass transfer model has been established to simulate the CO_2 diffusion through the immiscible interface, oil-CO_2 competitive adsorption on mineral surfaces, and oil swelling. The effect of dissolved CO_2 and adsorption on the oil-CO_2-solid three-phase contact angle is considered. Subsequently, the innovative model is verified by the microfluidic experiment. Comparative analysis of miscible and immiscible diffusion and competitive adsorption follows, focusing on the diffusion/dissolution of CO_2 droplets and oil-CO_2 competitive adsorption on mineral surfaces. Finally, the diffusion/dissolution of CO_2 into the porous media-saturated oil phase is simulated, and the effects of equilibrium dissolution concentration and CO_2 adsorption capacity on CO_2 diffusion/dissolution and oil swelling are studied.

2. Methodology based lattice Boltzmann model

2.1. Multicomponent and multiphase flow model

In our previous work, a two-component two-distribution MRT LBM was constructed to investigate the oil-CO_2 miscible diffusion and competitive adsorption processes under pressure conditions exceeding the MMP [17]. As shown in the schematic diagram of miscible diffusion in Fig. 1A, there is no distinct phase interface between CO_2 and oil phase. When the simulation system stabilizes, oil and CO_2 become completely miscible, and the amount of CO_2 dissolved in the oil phase cannot be controlled. When the pressure is below the MMP, the oil and CO_2 phases form an immiscible system with a clear interface. CO_2 has an equilibrium dissolution concentration in the oil phase, allowing it to diffuse into the oil phase region through the immiscible oil-CO_2 interface until the dissolved concentration reaches this equilibrium value at different temperatures and pressures. The diffusion of CO_2 droplets into the oil phase through the immiscible interface is depicted in Fig. 1B, with the diffusion direction indicated by the solid arrow. At this time, the whole system consists of two phases: CO_2 droplets (immiscible CO_2) and the miscible oil-CO_2 phase (a mixture of oil and dissolved CO_2). The novelty of the proposed methodology compared to previous works is summarized in Table 1.

A two-phase two-component three-distribution MRT LBM based on Shan-Chen schema is developed to capture the interfacial characteristics of immiscible oil-CO_2 and the competitive adsorption behavior of oil and dissolved CO_2. The three distribution functions correspond to oil, immiscible CO_2, and dissolved CO_2. Fig. 1B illustrates that the two of three-distribution governing equations are applied to describe the immiscible behavior of oil and CO_2. Since the mass transfer model cannot describe the adsorption of dissolved CO_2, the third governing equation is used to characterize the dissolved CO_2 in the oil phase, thereby enabling the capture of competitive adsorption behaviors. The general form of the governing equation is given as follows [52].

$$\mathbf{m}_\sigma^* = \mathbf{m}_\sigma - \mathbf{\Lambda}\left(\mathbf{m}_\sigma - \mathbf{m}_\sigma^{eq}\right) + \delta_t\left(\mathbf{I} - \frac{\mathbf{\Lambda}}{2}\right)\mathbf{S}_\sigma + \mathbf{M}\delta_t R_{\sigma,s} \tag{1}$$

where $\mathbf{m}_\sigma^* = \mathbf{M}\mathbf{f}_\sigma(\mathbf{x} + \mathbf{e}_\alpha\delta_t, t + \delta_t)$, $\mathbf{m}_\sigma = \mathbf{M}\mathbf{f}_\sigma(\mathbf{x}, t)$, $\mathbf{m}_\sigma^{eq} = \mathbf{M}\mathbf{f}_\sigma^{eq}$ are the density distribution function for the moments, $\mathbf{f}_\sigma$ is the density distribution function at position $\mathbf{x}$ and time t, δ_t is the time step, σ represents different components, and $\sigma = o, c-o, c$ represents oil phase, dissolved CO_2 in the oil phase, and immiscible CO_2 phase respectively, $\alpha = 0, 1, 2, \ldots 8$ is the velocity directions, $\mathbf{f}_\sigma^{eq}$ is the equilibrium density distribution function, $\mathbf{I}$ is the unit tensor, $\mathbf{\Lambda} = \left(\tau_\rho^{-1}, \tau_e^{-1}, \tau_\varsigma^{-1}, \tau_j^{-1}, \tau_q^{-1}, \tau_j^{-1}, \tau_q^{-1}, \tau_\nu^{-1}, \tau_\nu^{-1}\right)$ is the relaxation diagonal matrix, and $\tau_\rho^{-1} = \tau_j^{-1} = 1$, $\tau_e^{-1} = \tau_\varsigma^{-1} = \tau_q^{-1} = 1.1$, $\tau_\nu^{-1} = 1/\tau$ in our simulation,$\tau = \nu/\left(c_s^2\delta_t\right) + 0.5$ is relaxation time related to the multiphase and multicomponent flow, ν is lattice kinematic viscosity, $c_s = 1/\sqrt{3}$ is sound speed, $R_{\sigma,s}$ is the source term related to the phase change. $\mathbf{M}$ is the transformation matrix,

$$\mathbf{M} = \begin{bmatrix} 1 & 1 & 1 & 1 & 1 & 1 & 1 & 1 & 1 \\ -4 & -1 & -1 & -1 & -1 & 2 & 2 & 2 & 2 \\ 4 & -2 & -2 & -2 & -2 & 1 & 1 & 1 & 1 \\ 0 & 1 & 0 & -1 & 0 & 1 & -1 & -1 & 1 \\ 0 & -2 & 0 & 2 & 0 & 1 & -1 & -1 & 1 \\ 0 & 0 & 1 & 0 & -1 & 1 & 1 & -1 & -1 \\ 0 & 0 & -2 & 0 & 2 & 1 & 1 & -1 & -1 \\ 0 & 1 & -1 & 1 & -1 & 0 & 0 & 0 & 0 \\ 0 & 0 & 0 & 0 & 0 & 1 & -1 & 1 & -1 \end{bmatrix} \tag{2}$$

$\mathbf{S}_\sigma$ is the forcing term in the moment space, and the external total force is defined by $\mathbf{F}_\sigma = \mathbf{M}^{-1}\left(\mathbf{I} - \frac{\Lambda}{2}\right)\mathbf{S}_\sigma$,

$$\mathbf{S}_\sigma = \begin{bmatrix} 0 \\ 6\left(u_{\sigma,x}^{eq}F_{\sigma,x} + u_{\sigma,y}^{eq}F_{\sigma,y}\right) \\ -6\left(u_{\sigma,x}^{eq}F_{\sigma,x} + u_{\sigma,y}^{eq}F_{\sigma,y}\right) \\ F_{\sigma,x} \\ -F_{\sigma,x} \\ F_{\sigma,y} \\ -F_{\sigma,y} \\ 2\left(u_{\sigma,x}^{eq}F_{\sigma,x} - u_{\sigma,y}^{eq}F_{\sigma,y}\right) \\ \left(u_{\sigma,x}^{eq}F_{\sigma,y} + u_{\sigma,y}^{eq}F_{\sigma,x}\right) \end{bmatrix} \tag{3}$$

The equilibrium velocity in **Eq. (3)** is expressed as

$$\mathbf{u}_\sigma^{eq} = \frac{\sum_\sigma \rho_\sigma \mathbf{u}_\sigma}{\sum_\sigma \rho_\sigma} \tag{4}$$

where ρ_σ is the density with $\rho_\sigma = \sum_\alpha f_{\sigma,\alpha}$, $\mathbf{u}_\sigma$ is velocity of component σ, and is given by

$$\mathbf{u}_\sigma = \left(u_{\sigma,x}, u_{\sigma,y}\right) = \frac{\sum_\alpha \mathbf{e}_\alpha f_{\sigma,\alpha} + 0.5\delta_t\mathbf{F}_\sigma}{\rho_\sigma} \tag{5}$$

In the simulation of a multicomponent system, three primary interaction forces are employed, that include the fluid-fluid interaction force ($\mathbf{F}_{\sigma,int}$), which captures the interfacial characteristic, the fluid-solid interaction force ($\mathbf{F}_{\sigma,\mathrm{ads}}$), which controls the wettability and the adsorption, and the body force ($\mathbf{F}_{\sigma,\mathrm{b}}$), which drives the fluid flow. Consequently, the external total force can be redefined as $\mathbf{F}_\sigma =$

$(F_{\sigma,x}, F_{\sigma,y}) = \mathbf{F}_{\sigma,int} + \mathbf{F}_{\sigma,\mathrm{ads}} + \mathbf{F}_{\sigma,\mathrm{b}}$.

The fluid-fluid interaction force $\mathbf{F}_{\sigma,int}$ is given by [50].

$$\mathbf{F}_{\sigma_1,int}(\boldsymbol{x},t) = -\psi_{\sigma_1}(\boldsymbol{x}) \begin{bmatrix} G_{\sigma_1,\sigma_1}\sum_{\alpha} w\left(|\mathbf{e}_\alpha|^2\right)\psi_{\sigma_1}(\boldsymbol{x}+\mathbf{e}_\alpha\delta_t)\mathbf{e}_\alpha \\ +G_{\sigma_1,\sigma_2}\sum_{\alpha} w\left(|\mathbf{e}_\alpha|^2\right)\psi_{\sigma_2}(\boldsymbol{x}+\mathbf{e}_\alpha\delta_t)\mathbf{e}_\alpha \\ +G_{\sigma_1,\sigma_3}\sum_{\alpha} w\left(|\mathbf{e}_\alpha|^2\right)\psi_{\sigma_3}(\boldsymbol{x}+\mathbf{e}_\alpha\delta_t)\mathbf{e}_\alpha \end{bmatrix}, \tag{6}$$

where $\psi_{\sigma_1} = 1 - exp(-\rho_{\sigma_1})$ is a pseudopotential, $w\left(|\mathbf{e}_\alpha|^2\right)$ is the weight, and $w(1) = 1/3$, $w(2) = 1/12$. G_{σ_1,σ_1} is an interaction parameter of the same fluid, G_{σ_1,σ_2} and G_{σ_1,σ_3} are the fluid-fluid interaction parameters controlling phases separation and miscibility, for oil-dissolved CO_2, oil-immiscible CO_2, and dissolved CO_2-immiscible CO_2, the interaction parameters are $G_{o,c-o} = 1$, $G_{o,c} = 2.1$, $G_{c,c-o} = 2.1$, respectively.

To capture the ideal wettability of oil and immiscible CO_2, the fluid-solid interaction force $\mathbf{F}_{\sigma,ads}$ of oil and immiscible CO_2 can be expressed as [58].

$$\mathbf{F}_{\sigma,\mathrm{ads}}(\mathbf{x},t) = -G_{\sigma,\mathrm{ads}}\psi_\sigma(\mathbf{x},t)\sum_{\alpha} w\left(|\mathbf{e}_\alpha|^2\right)s_f(\mathbf{x}+\mathbf{e}_\alpha\delta_t)\mathbf{e}_\alpha, \tag{7}$$

where $G_{\sigma,\mathrm{ads}}$ is a fluid-solid interaction parameter and expressed by $G_{o,\mathrm{ads}}$ and $G_{c,\mathrm{ads}}$ for oil and immiscible CO_2, s_f is an indicator parameter that equals 0 and 1 for fluid and solid regions, respectively.

Eq. (7) is exclusively applied to both the oil phase and immiscible CO_2 phase. To simulate the competitive adsorption behaviors between oil and dissolved CO_2, an exponential force scheme is employed to characterize the dissolved CO_2-solid interaction force $\mathbf{F}_{c-o,\mathrm{ads}}$ at various positions, where the interaction force decreases with increasing distance from the solid surface. Meanwhile, **Eq. (7)** is applied to fix the oil-solid interaction force value, and then the competitive adsorption of the oil phase and dissolved CO_2 can be modeled. The dissolved CO_2-solid interaction force is shown below [59].

$$\mathbf{F}_{c-o,\mathrm{ads}}(\mathbf{x},t) = -G_{c-o,\mathrm{ads}}\psi(\mathbf{x},t)\sum_{\alpha} e^{-|\mathbf{x}_\alpha|/\lambda}\mathbf{e}_\alpha, \tag{8}$$

where $G_{c-o,\mathrm{ads}}$ is a CO_2-solid interaction parameter, $\mathbf{x}_\alpha$ is the distance from the solid surface in direction α. Immiscible CO_2 is assumed to not adsorb on mineral surfaces, while only dissolved CO_2 can adsorb, thus competing with the oil phase for adsorption. Therefore, **Eq. (8)** is exclusively used to calculate the dissolved CO_2-solid interaction force in the oil phase.

2.2. Mass transfer model

To describe the process of CO_2 diffusion/dissolution in the oil phase, the LB model with D2Q5 scheme is applied [60], and the evolution equation is given by

$$g_\alpha(\mathbf{x}+\mathbf{e}_\alpha\delta_t, t+\delta_t) - g_\alpha(\mathbf{x},t) = -\frac{1}{\tau_g}\left(g_\alpha(\mathbf{x},t) - g_\alpha^{eq}(\mathbf{x},t)\right), \tag{9}$$

where g_α is the concentration distribution function for the dissolved CO_2, τ_g is relaxation time related to the CO_2 diffusion, $\alpha = 0, 1, 2, \ldots, 4$ is the velocity directions of the D2Q5 model, g_α^{eq} is the equilibrium dissolution concentration distribution function,

$$g_\alpha^{eq} = C\left[J_\alpha + \frac{1}{2}\mathbf{e}_\alpha\cdot\mathbf{u}\right], \tag{10}$$

where $C = \sum g_\alpha$ is CO_2 solution concentration, J_α is calculated by the rest fraction method, and is shown below [60].

$$J_\alpha = \begin{cases} J_0 & \alpha = 0 \\ (1-J_0)/4 & \alpha = 1,2,3,4 \end{cases}, \tag{11}$$

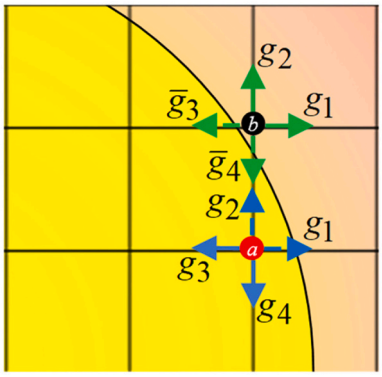

Fig. 2. The enlarged image of region A in Fig. 1, shows the immiscible oil-CO_2 interfacial region and grid distribution.

where J_0 is a free parameter ranging from 0 to 1.

The effective diffusion coefficient of CO_2 is defined by **Eq. (12)**, and the validation of the mass transfer model can be found in our previous study [57].

$$D = \frac{1}{2}(1-J_0)(\tau_g - 0.5) \tag{12}$$

2.3. Phase change on oil-CO_2 interface

The dissolved concentration of CO_2 at the oil-CO_2 interface is governed by Henry's law, as demonstrated in **Eq. (13)**. The subscript *co* represents the immiscible oil-CO_2 interface region, *c-co* is the CO_2 phase which is a single-layer lattice near the oil phase, and as shown at point *a* in Fig. 2. Fig. 2 provides an enlarged view and lattice distribution of region A in Fig. 1. The oil-immiscible CO_2 interface is determined by the free parameter density threshold.

$$C_{eq}|_{c-co} = H\cdot p_{CO_2}, \tag{13}$$

where C_{eq} is the equilibrium concentration of dissolved CO_2 under specific pressure and temperature conditions. The CO_2 concentration in a single-layer lattice near the oil phase is ensured a constant value C_{eq} until the concentration of dissolved CO_2 is equal to C_{eq}.

During the process of CO_2 dissolution, the dissolved CO_2 contributes to the decrease of the immiscible CO_2 mass $\rho_{c-co} = \sum_\alpha f_{c-co,\alpha}$, and the increase of dissolved CO_2 mass $\rho_{co-o} = \sum_\alpha f_{co-o,\alpha}$ at two adjacent time steps, *co-o* is a single-layer lattice which is in the oil phase and near the CO_2 phase, and the location is shown at point *b* in Fig. 2. For the percentage of mass decrease or increase at the *c-co* and *co-o* region, we proportionally decrease or increase the density distribution function in 9 directions of the corresponding lattice. Consequently, the source term for immiscible CO_2 and dissolved CO_2 in the oil phase in **Eq. (1)** can be calculated as

$$R_{c,s}|_{c-co} = -f_{c,\alpha}\left(\left(\sum_\alpha\left(C_{eq}J_\alpha s_{g1}(\mathbf{x}-\mathbf{e}_\alpha\delta_t) - g_\alpha s_{g1}(\mathbf{x}+\mathbf{e}_\alpha\delta_t)\right)M_c\right)\Big/\sum_\alpha f_{c,\alpha}\right), \tag{14}$$

$$R_{c-o,s}|_{co-c} = f_{c-o,\alpha}\left(\left(\sum_\alpha\left(g_\alpha s_{g2}(\mathbf{x}+\mathbf{e}_\alpha\delta_t) - \overline{g_\alpha} s_{g2}(\mathbf{x}-\mathbf{e}_\alpha\delta_t)\right)M_c\right)\Big/\sum_\alpha f_{c-o,\alpha}\right), \tag{15}$$

where s_{g1} and s_{g2} are the indicator parameters, and s_{g1} equals 1 and 0 for the regions of oil and CO_2 phase, s_{g2} equals 0 and 1 for the regions of oil and CO_2 phase, $\overline{g_{co-o,\alpha}}$ is the post-collision and pre-migration concentration distribution function. Using points *a* and *b* in Fig. 2 as examples,

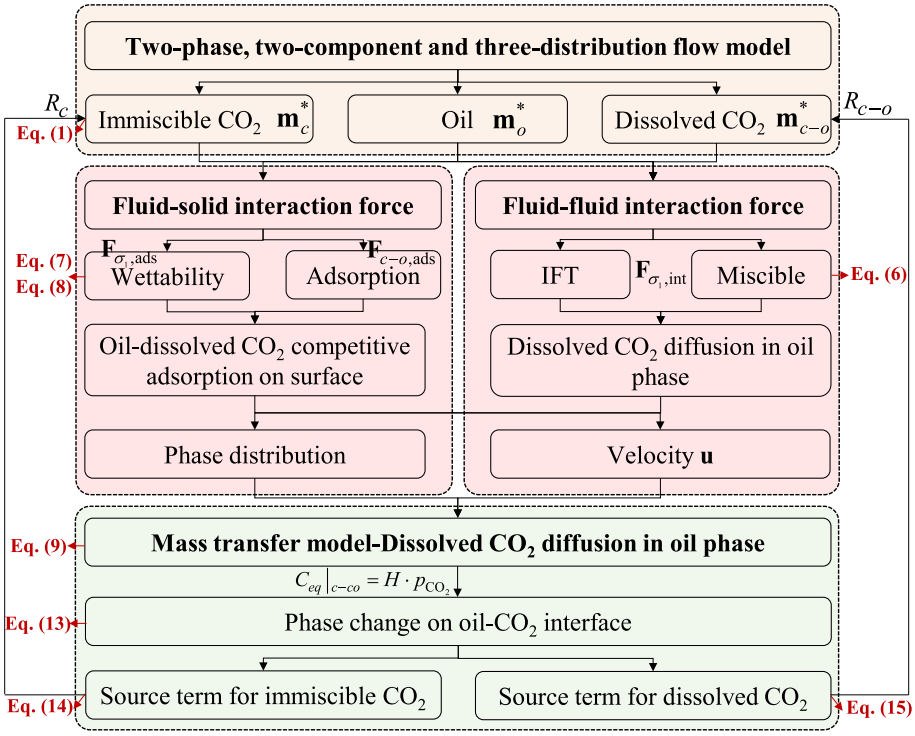

Fig. 3. Workflow of simulation.

Eqs. (14) and (15) can be reduced to **Eqs. (16) and (17)**. At point a, $g_1 = C_{eq}J_1$ and $g_2 = C_{eq}J_2$ are concentration distribution functions calculated by equilibrium dissolution concentration, and after migration, they diffuse into the oil phase region, resulting in a decrease in CO_2 concentration. g_3 and g_4 are migrated from the oil phase region, increasing CO_2 concentration. Therefore, the net decrease value in the CO_2 concentration at point a is $C_{eq}J_1 + C_{eq}J_2 - g_3 - g_4$, then, according to the net decrease value, the density distribution function $f_{c,\alpha}\big|_a$ of point a in 9 directions is reduced in equal proportion. At point b, g_1 and g_2 are migrated from the immiscible CO_2 region, increasing CO_2 concentration. $\bar{g}_3$ and $\bar{g}_4$ are the concentration distribution function that migrates into the immiscible CO_2 phase, causing the concentration value to decrease. Therefore, the net increase value in the CO_2 concentration at point b is $g_1 + g_2 - \bar{g}_3 - \bar{g}_4$, then the net increase value is distributed proportionally to the density distribution function $f_{c-o,\alpha}\big|_b$ in the 9 directions of point b.

$$R_{c,s}\big|_a = -f_{c,\alpha}\left(\left((C_{eq}J_1 + C_{eq}J_2 - g_3 - g_4)M_c\right)\Big/\sum_\alpha f_{c,\alpha}\right). \tag{16}$$

$$R_{c-o,s}\big|_b = f_{c-o,\alpha}\left(\left((g_1 + g_2 - \bar{g}_3 - \bar{g}_4)M_c\right)\Big/\sum_\alpha f_{c-o,\alpha}\right). \tag{17}$$

The adsorption effect on the solid surface significantly influences the CO_2 dissolution [17]. Since the adsorption effect of CO_2 cannot be considered by the mass transfer model, when the CO_2 concentration reaches the equilibrium dissolution concentration C_{eq}, the equilibrium dissolution concentration of CO_2 in the flow model is lower than the given equilibrium dissolution concentration C_{eq} due to the substantial amount of CO_2 adsorbed near the solid surface. To ensure that CO_2 continues to diffuse in the mass transfer model, it is necessary to modify the CO_2 concentration in the adsorption region based on the adsorption effect calculated by the flow model. First, the adsorption effect is simulated by **Eq. (8)** to determine if the adsorption concentration exceeds the equilibrium dissolution concentration. If the adsorption concentration is greater than a certain difference value, the CO_2 concentration at the corresponding position in the mass transfer model decreases the corresponding difference value. This difference value is proportionally allocated to the concentration distribution function in five directions. As a result, the equilibrium dissolution concentration of CO_2 in the multicomponent multiphase flow model is effectively guaranteed to be equal to the given equilibrium dissolution concentration C_{eq}.

2.4. Workflow of simulation

In the simulation, lattice and physical units are converted using the constants for length scale $L_0 = 1 \times 10^{-10}$ m, time scale $T_0 = 2 \times 10^{-15}$ s and mass scale $M_0 = 8 \times 10^{-28}$ kg. Throughout this paper, lattice units are consistently denoted as "lu". In the multicomponent and multiphase flow model, the CO_2 concentration in the oil phase is expressed as $C_{co_2} = \sum_\alpha f_{c-o,\alpha}\frac{M_0}{L_0^3}\frac{1}{1000M_c}$ mol/L, where $M_c = 0.044$ kg/mol represents CO_2 molar mass. To facilitate the calculation of the source term between the flow model and the mass transfer model, the density distribution is utilized in the mass transfer model. Consequently, the concentration distribution in the mass transfer model can be derived from the density distribution $C_{co_2} = \sum_\alpha g_\alpha\frac{M_0}{L_0^3}\frac{1}{1000M_c}$ mol/L. Additionally, we assume that lattice densities (ρ_l) of both oil and immiscible CO_2 are equal to 1 lu, with the corresponding physical density denoted as $\rho_p = 1 \times \frac{M_0}{L_0^3} = 800$ kg/m^3. The methodology demonstrates excellent scalability and adaptability, making it well-suited for studying the phase behavior of CO_2 and realistic crude oil. Since the original LB model based on the Shan-Chen schema cannot accurately characterize the high oil-CO_2 density ratio, a realistic crude oil-CO_2 density ratio under different pressure and temperature conditions can be achieved by incorporating an equation of state (such as Peng-Robinson and Carnahan-Starling) to the fluid-fluid interaction force $\mathbf{F}_{\sigma,int}$ [8,61,62]. Subsequently, the equilibrium dissolution concentration and diffusion coefficient of CO_2 in crude oil under varying temperature and pressure conditions can be

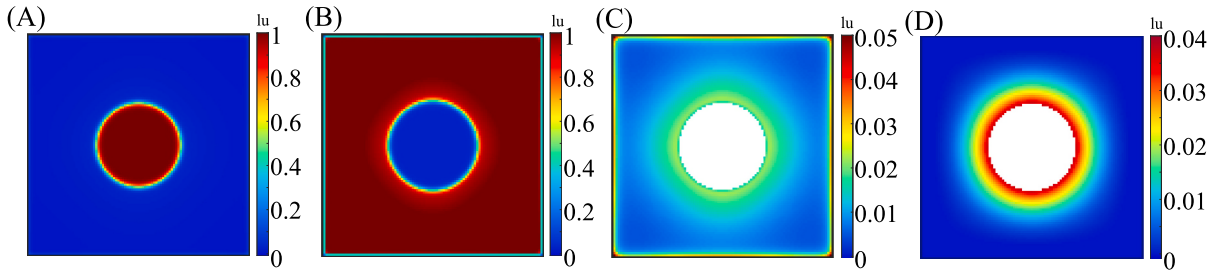

Fig. 4. Component and phase distribution. (A) Density distribution of immiscible CO_2 droplets based on **Eq. (1)**, and physical density is $\rho_p = \rho_l \times \frac{M_0}{L_0^3}$, (B) Density distribution of oil phase based on **Eq. (1)**, (C) Concentration distribution of dissolved CO_2 in the oil phase based on **Eq. (1)**, and the physical concentration distribution can be defined by $C_{co_2} = \sum_\alpha f_{c-o,\alpha} \frac{M_0}{L_0^3} \frac{1}{1000 M_c}$ mol/L, (D) Concentration distribution of dissolved CO_2 based on **Eq. (9)**, and the physical concentration distribution is $C_{co_2} = \sum_\alpha g_\alpha \frac{M_0}{L_0^3} \frac{1}{1000 M_c}$ mol/L.

determined using molecular simulation or experimental methods [34,63]. Finally, the diffusion/dissolution and competitive adsorption behaviors of CO_2 in realistic crude oil can then be simulated according to the modified model with the equilibrium dissolution concentration and diffusion coefficient. Meanwhile, the methodology is applicable to studying the oil-phase behavior in various oil reservoirs, including shale oil, tight sandstone oil, and conventional sandstone oil reservoirs. In conventional sandstone porous media, the pore size is significantly larger than the molecular size, allowing the adsorption effect of oil-CO_2 on mineral surfaces to be neglected. Thus, the corresponding simulation can be conducted by adjusting the fluid-solid interaction force parameter $G_{c-o,\mathrm{ads}}$ in Eq. (8) to 0.

The workflow of the simulation and the corresponding equations are depicted in Fig. 3. First, the phase distribution and velocity of immiscible CO_2, oil, and dissolved CO_2 are calculated by the three-distribution Shan-Chen LB flow model. In the flow model, wettability and competitive adsorption are captured by fluid-solid interaction force, while immiscible interfacial tension (IFT) and miscible behavior are captured by the fluid-fluid interaction force. Based on the physical model in Fig. 1B, a CO_2 droplet is positioned within the oil phase and the peripheral boundary is the solid boundary. The calculation results of the flow model are shown in Fig. 4A-C, where **(A)** shows the density distribution of immiscible CO_2, **(B)** shows the density distribution of the oil phase, and **(C)** shows the concentration distribution of dissolved CO_2 in the oil phase. The dissolved CO_2 gradually diffuses from the immiscible oil-CO_2 interface into the oil phase and is adsorbed on solid surfaces. Next, a mass transfer model is employed to simulate the CO_2 diffusion through the oil-CO_2 interface. The results are depicted in Fig. 4D, where the equilibrium dissolution concentration is 0.04 lu. Therefore, the CO_2 concentration at the oil-CO_2 interface is 0.04 lu, and CO_2 gradually diffuses into the oil phase due to the concentration difference. The source term of immiscible CO_2 and dissolved CO_2 in the flow model is calculated based on the diffusion amount, ensuring precise control over the CO_2 dissolution rate and equilibrium dissolution concentration.

3. Model verification

3.1. Contact angle

The contact angle between immiscible CO_2 and oil phase is governed by **Eq. (7)**, where the relationship between the oil-solid interaction force ($G_{o,\mathrm{ads}}$) and CO_2-solid interaction force ($G_{c,\mathrm{ads}}$) in **Eq. (7)** is $G_{o,\mathrm{ads}} = -G_{c,\mathrm{ads}}$. Without considering CO_2 dissolution in the oil phase, the dependence of immiscible CO_2 contact angle on the CO_2-solid interaction force ($G_{c,\mathrm{ads}}$) is illustrated in Fig. 5A. By selecting the appropriate $G_{c,\mathrm{ads}}$, the desired wettability characteristics can be obtained. Then, the immiscible CO_2 contact angles of 26.48° and 122.20° are selected to conduct the simulations of CO_2 dissolution in the oil phase, exploring the effects of dissolved CO_2 on the immiscible CO_2 contact angles. As shown in Fig. 5B, with the increase of CO_2 diffusion time, the concentration of dissolved CO_2 in the oil phase increases, leading to an increase in the immiscible CO_2 contact angle, which can be explained by Young's equation and surface adhesion. Without considering the CO_2 diffusion/dissolution in the oil phase, the immiscible CO_2 contact angle can be

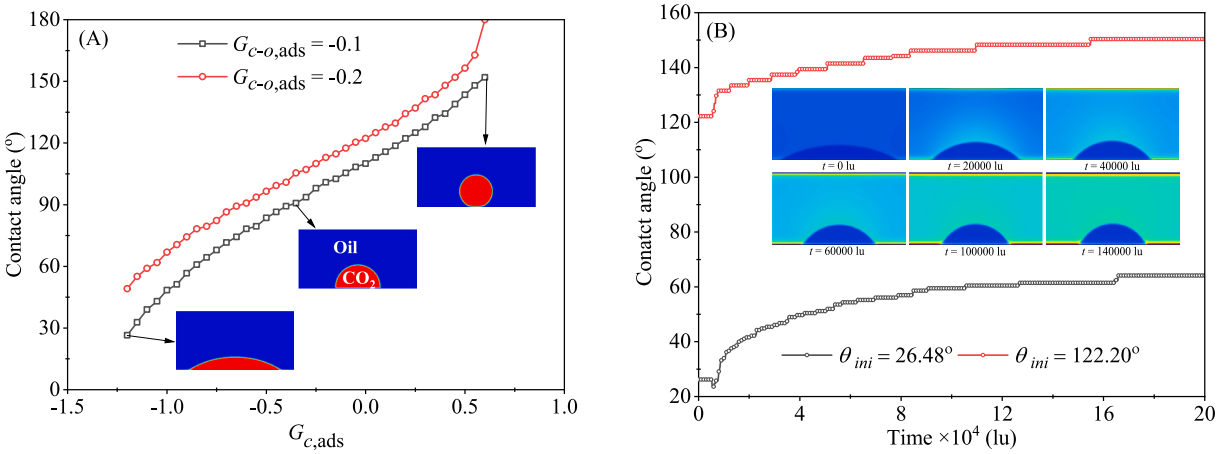

Fig. 5. The variation of contact angle with CO_2-solid interaction force parameter $G_{c,\mathrm{ads}}$, adsorption capacity $G_{c-o,\mathrm{ads}}$ and CO_2 diffusion time. (A) CO_2-solid interaction foece parameter $G_{c,\mathrm{ads}}$ and adsorption capacity $G_{c-o,\mathrm{ads}}$ without considering CO_2 diffusion and dissolution in the oil phase; (B) CO_2 diffusion time considering CO_2 diffusion and dissolution in the oil phase, and the inset figure is the distribution of CO_2 concentration in the oil phase. The physical time t_p can be expressed as $t_p = t \times T_0$, t is lattice time.

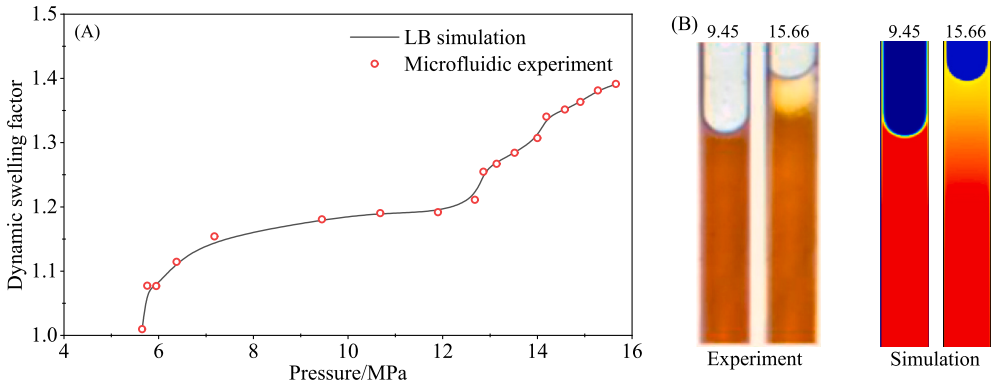

Fig. 6. Comparison between the swelling factor calculated by LB simulation and microfluidic experiment [17]. (A) Dynamic swelling factor versus pressure; (B) the density distribution of oil phase at pressures of 9.45 MPa and 15.66 MPa.

characterized by Young's equation $cos\theta = (\gamma_{so} - \gamma_{sc})/\gamma_{co}$, where γ_{so} and γ_{sc} are the oil-solid and immiscible CO_2-solid surface tension, γ_{co} is the oil-CO_2 interfacial tension between the oil and immiscible CO_2 phases. The fluid-solid surface tension approximates the fluid-solid surface adhesion, which is defined by the attraction between the fluid-solid molecular species [64]. As CO_2 diffuses into the oil phase, the adsorption capacity of CO_2 is greater than that of the oil phase, resulting in an increase in surface adhesion between the oil-dissolved CO_2 phase and the solid, which consequently increases the surface tension. According to Young's equation, as γ_{so} increases, the contact angle increases. Due to the particularity of LB simulation based on the Shan-Chen scheme, a small amount of immiscible CO_2 is dissolved in the oil phase to stabilize the model. Therefore, due to the enhancement of the fluid-solid force of immiscible CO_2 (the smaller the $G_{c-o,ads}$ value, the stronger the adsorption capacity of dissolved CO_2), the CO_2 contact angle will increase, as shown in Fig. 5A.

3.2. Verification with microfluidic experiment

The competitive adsorption validation of the proposed model can be found in our previous studies [17]. In this paper, only CO_2 dissolution and oil swelling behavior are verified. The results from the microfluidic experiment are then used to verify the proposed model excluding competitive adsorption. Recently, a microfluidic experiment was conducted to investigate the swelling effect during CO_2 dissolution in the oil phase with CO_2 pressure ranging from 5.11 MPa to 15.66 MPa [65]. The swelling degree is expressed by the swelling factor, which is defined as the ratio of the oil volume after swelling to the oil phase volume at 5.11 MPa pressure. In the simulation process, we first set the equilibrium dissolution concentration of dissolved CO_2 to 10.896 mol/L when the CO_2 pressure is 15.66 MPa, and then simulate CO_2 diffusion and oil swelling. When the lattice time is equal to 364,000 lu, the swelling factor approximates the experimental swelling factor of 1.39. Then, according to Henry's law $C_{eq}|_{c-co} = H \cdot p_{CO_2}$, the CO_2 equilibrium dissolution concentration is proportional to the CO_2 pressure, and the corresponding dissolution equilibrium dissolution concentration is determined to range from 3.54 mol/L to 10.90 mol/L with pressure varying from 5.11 MPa to 15.66 MPa. The simulation is then conducted using the corresponding equilibrium dissolution concentration of CO_2 under different pressures to achieve a perfect match between the simulated swelling factor and the experimental swelling factor. The results, presented in Fig. 6, indicate that the proposed model can successfully capture the phenomenon of CO_2 diffusion and oil swelling.

4. Results and discussion

4.1. Miscible and immiscible diffusion and adsorption

In our previous work, the oil-CO_2 miscible diffusion and competitive adsorption processes were investigated [17]. As depicted in Fig. 7, a simplified physical model of the oil-CO_2 system is established, featuring a central circular region representing CO_2, surrounded by oil. The lattice

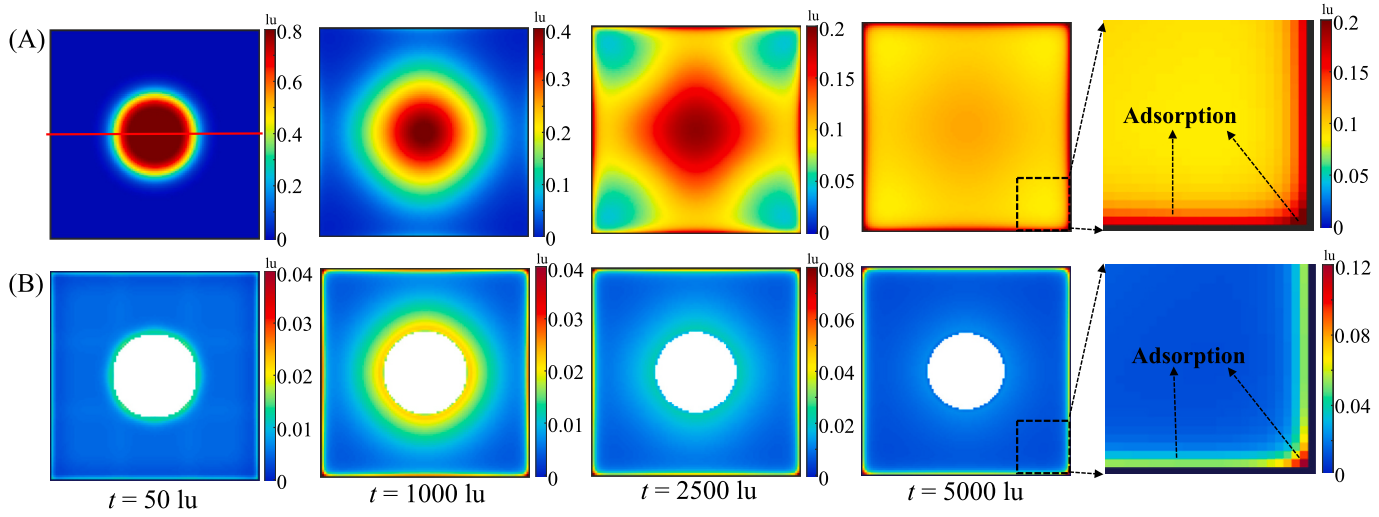

Fig. 7. The distribution of CO_2 concentration during CO_2 diffusion. (A) Miscible diffusion [17]; (B) immiscible diffusion, and the white circular region represents immiscible CO_2 droplets.

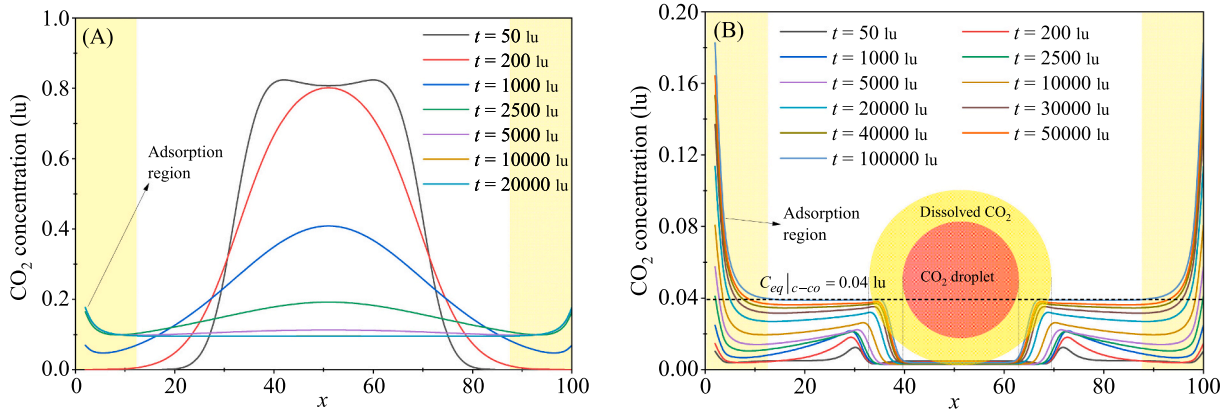

Fig. 8. The distribution curve of CO_2 concentration along the central axis of the model (red line in Fig. 7A) during CO_2 diffusion. (A) Miscible diffusion; (B) immiscible diffusion. (For interpretation of the references to colour in this figure legend, the reader is referred to the web version of this article.)

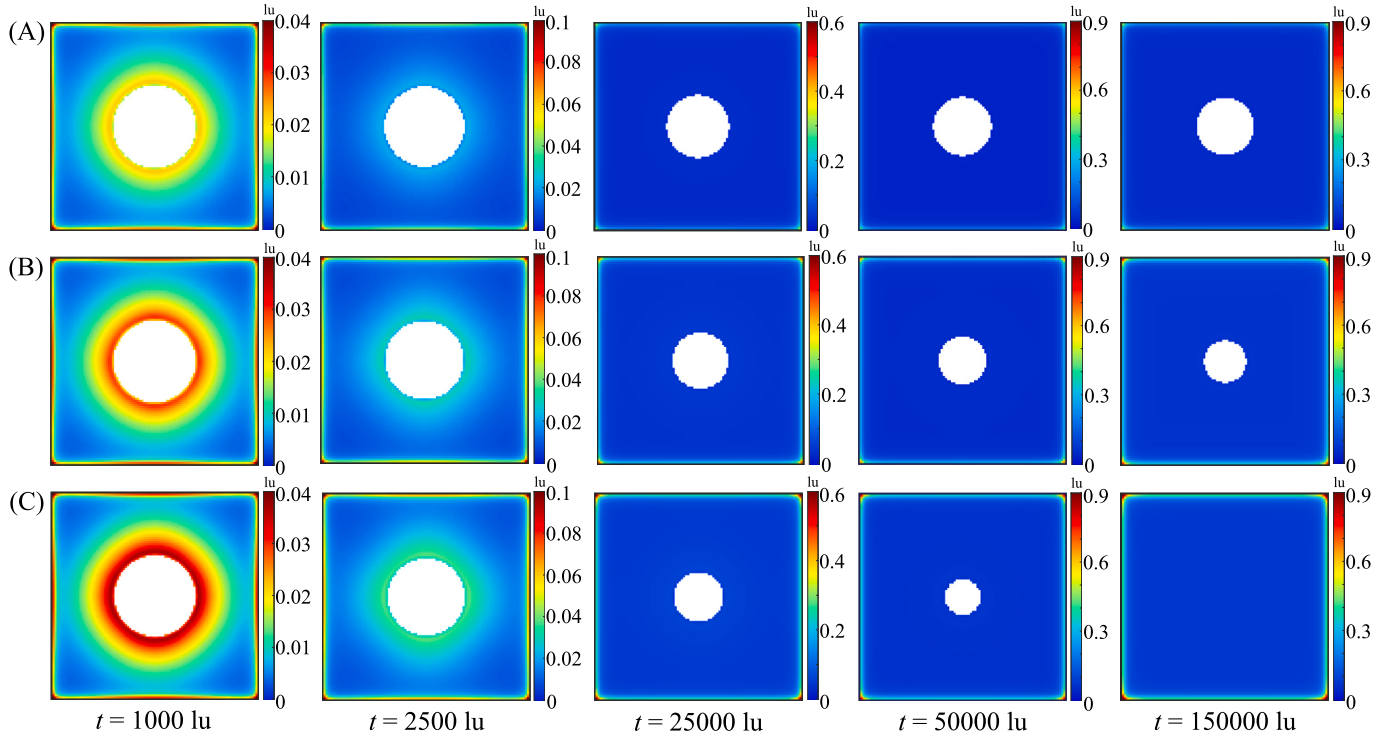

Fig. 9. The distribution of dissolved CO_2 concentration at different equilibrium dissolution concentrations. (A) $C_{eq}|_{c-co}$ = 0.04 lu = 0.73 mol/L; (B) $C_{eq}|_{c-co}$ = 0.06 lu = 1.09 mol/L, (C) $C_{eq}|_{c-co}$ = 0.08 lu = 1.46 mol/L.

size of the physical model is 100 × 100, corresponding to a physical size of 10 × 10 nm under the length scale of $L_0 = 1 \times 10^{-10}$ m. The four boundaries of the physical model are the solid, where the competitive adsorption of oil and dissolved CO_2 phases can occur. Fig. 7**A** and **B** illustrate the distribution of CO_2 concentration under the conditions of CO_2 miscible and immiscible diffusion, respectively. Fig. 8**A** and **B** show the distribution curve of dissolved CO_2 concentration along the central axis of the model. In Fig. 8B, the concentration of the immiscible CO_2 droplets is not considered. During miscible diffusion, there is no distinct oil-CO_2 interface. Competitive adsorption occurs on the solid surface, with the adsorption concentration of CO_2 gradually increasing over time. In immiscible diffusion, the equilibrium dissolution concentration of CO_2 is $C_{eq}|_{c-co}$ = 0.04 lu = 0.73 mol/L, and the dissolved CO_2-solid interaction force parameter is $G_{c-o,\text{ads}} = -0.1$, indicating that the adsorption capacity of dissolved CO_2 is greater than that of the oil phase. Then, as time increases, CO_2 gradually diffuses into the oil phase, leading to a decrease in the volume of CO_2 droplets. Simultaneously, the concentration of dissolved CO_2 in the oil phase, away from the solid, gradually increases and approaches the equilibrium dissolution concentration, while the adsorption concentration of CO_2 on the solid surface increases.

4.2. *Diffusion and dissolution of CO_2 droplets*

Subsequently, the same physical model, detailed in section **4.1 Miscible and immiscible diffusion and adsorption**, is applied to simulate the CO_2 droplets' diffusion/dissolution and competitive adsorption under varying equilibrium dissolution concentrations and adsorption capacities. Fig. 9 illustrates the distribution of dissolved CO_2 concentration under various equilibrium dissolution concentrations. As an increasing equilibrium dissolution concentration, it can be intuitively observed that the dissolved CO_2 concentration increases when lattice

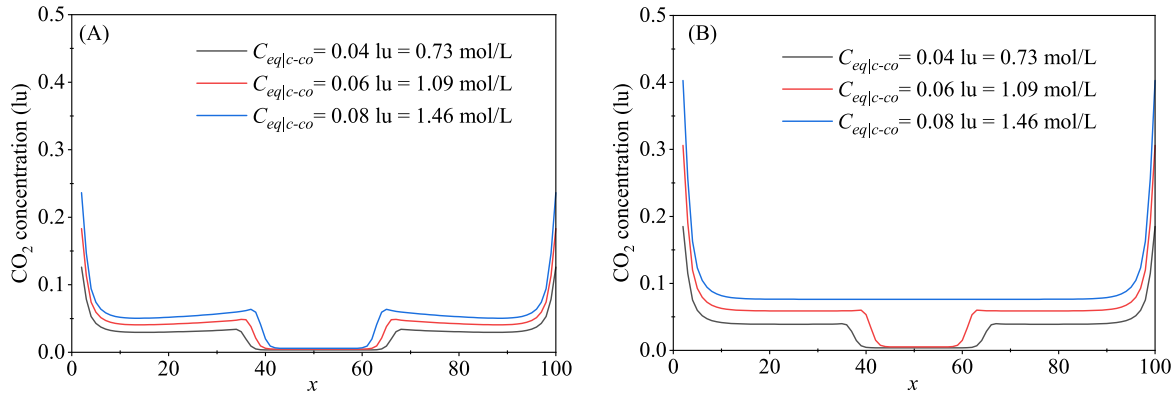

Fig. 10. The distribution curve of dissolved CO_2 concentration at different equilibrium dissolution concentrations. (A) t = 25000 lu; (B) t = 150000 lu.

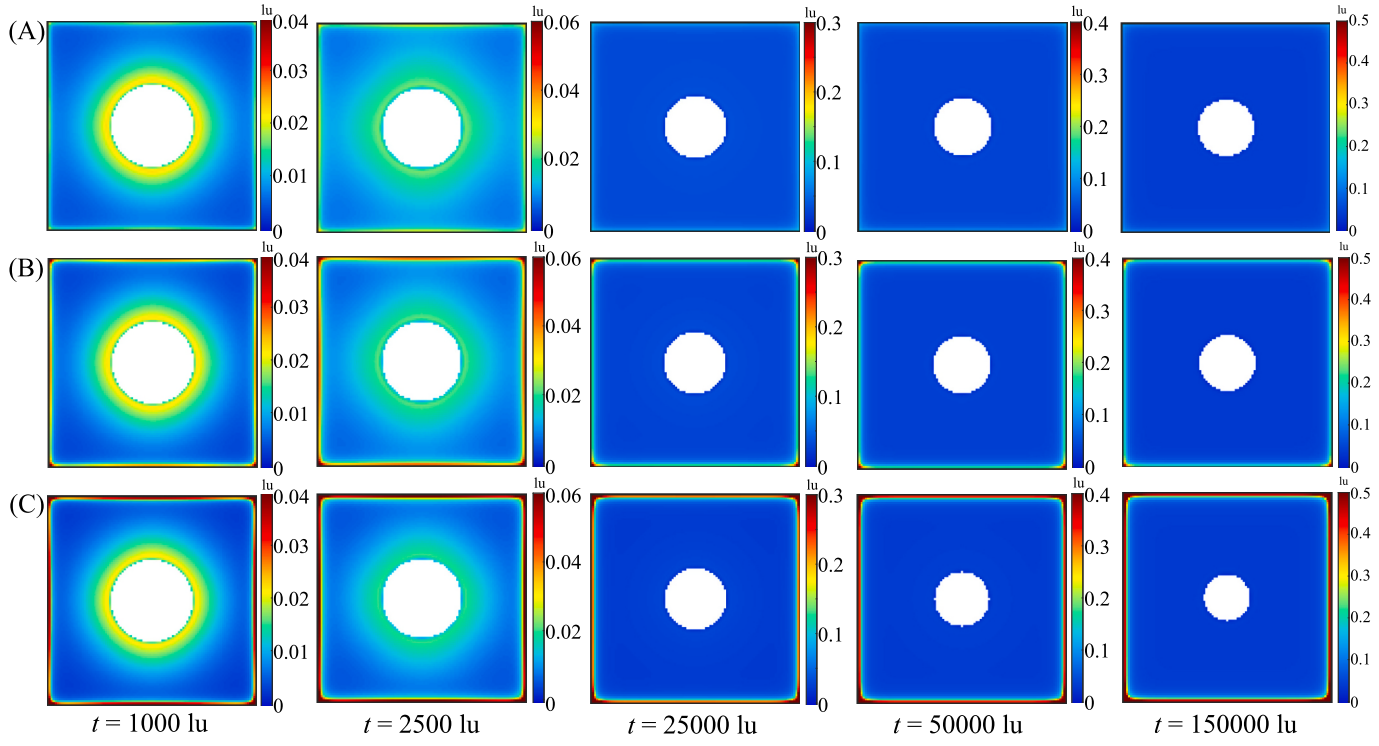

Fig. 11. The distribution of dissolved CO_2 concentration at different adsorption capacities. (A) $G_{c-o,\mathrm{ads}} = -0.05$; (B) $G_{c-o,\mathrm{ads}} = -0.1$, (C) $G_{c-o,\mathrm{ads}} = -0.15$.

time is equal to 1000 lu. Additionally, the dissolution rate of CO_2 increases and the volume of CO_2 droplets gradually decreases. When the

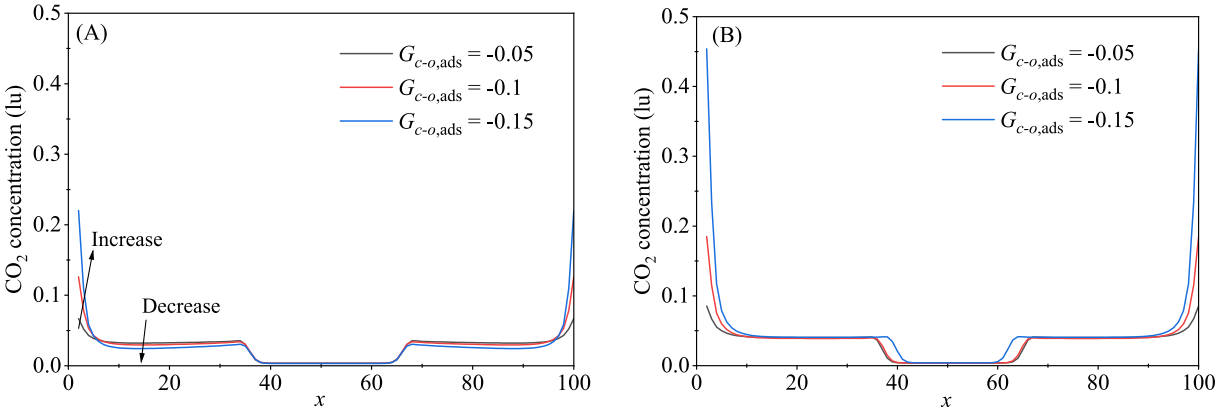

Fig. 12. The distribution curve of dissolved CO_2 concentration at different adsorption capacities. (A) t = 25000 lu; (B) t = 150000 lu.

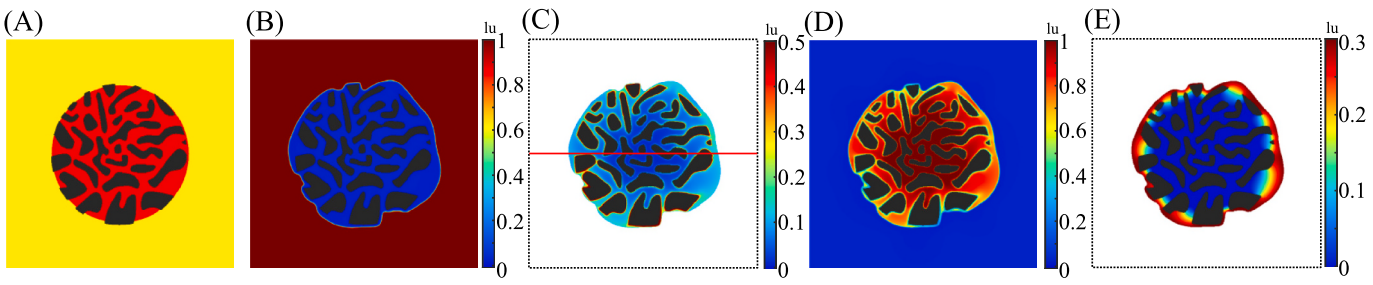

Fig. 13. Conceptual model, and oil-CO_2 density/concentration distribution with $C_{eq}|_{c-co} = 0.3$ lu $= 5.45$ mol/L, $G_{c-o,\text{ads}} = -0.1$ and $t = 10000$lu. (A) Conceptual model, red: oil phase, yellow: immiscible CO_2, black, solid matrix; (B) Density distribution of immiscible CO_2 based on **Eq.** (1); (C) Concentration distribution of dissolved CO_2 based on **Eq.** (1); (D) Density distribution of oil phase based on **Eq.** (1); (E) Concentration distribution of dissolved CO_2 based on **Eq.** (9). (For interpretation of the references to colour in this figure legend, the reader is referred to the web version of this article.)

equilibrium dissolution concentration is 0.04 lu = 0.73 mol/L and 0.06 lu = 1.09 mol/L, CO_2 droplets still exist after the system equilibrium. However, when the equilibrium dissolution concentration is 0.08 lu = 1.46 mol/L, CO_2 droplets are completely dissolved upon system equilibrium. Fig. 10 illustrates the dissolved CO_2 concentration along the central axis of the model (as indicated by the red line in Fig. 7A) under different equilibrium dissolution concentrations. As the equilibrium dissolution concentration increases, the dissolved CO_2 concentration in the bulk phase area gradually increases, while the adsorbed dissolved CO_2 concentration in the near-wall region also gradually increases.

When the CO_2 droplets gradually dissolve into the oil phase, the dissolved CO_2 diffuses driven by the concentration gradients. As dissolved CO_2 reaches the near-wall region, the strong fluid-solid interaction force promotes the competitive adsorption of oil and dissolved CO_2 phases, resulting in a higher concentration of dissolved CO_2 near the wall compared to the bulk region. Fig. 11 illustrates the distribution of dissolved CO_2 concentration at different dissolved CO_2 adsorption capacities. As the dissolved CO_2-solid interaction force parameter decreases from −0.05 to −0.15, the adsorption capacity for dissolved CO_2 increases. Consequently, the dissolved CO_2 concentration in the near-wall region gradually increases, as illustrated in Fig. 12. Meanwhile, because of the rapid adsorption of CO_2, the concentration of dissolved CO_2 in the bulk region decreases, as depicted in Fig. 12A. When the dissolved CO_2 concentration in the bulk region eventually equals the equilibrium dissolution concentration, the volume of CO_2 droplets decreases due to the increasing dissolved CO_2 adsorption capacity, resulting in more dissolved CO_2 adsorbed on the solid surface, as the distribution curve of dissolved CO_2 concentration given in Fig. 12B.

4.3. Effect of equilibrium dissolution concentration

According to the physical process of CO_2 huff and puff extraction of shale oil, a physical model is established to simulate this process. The physical model is shown in Fig. 13A, where the oil phase is saturated in the middle circular nanoporous media, and CO_2 is saturated around the

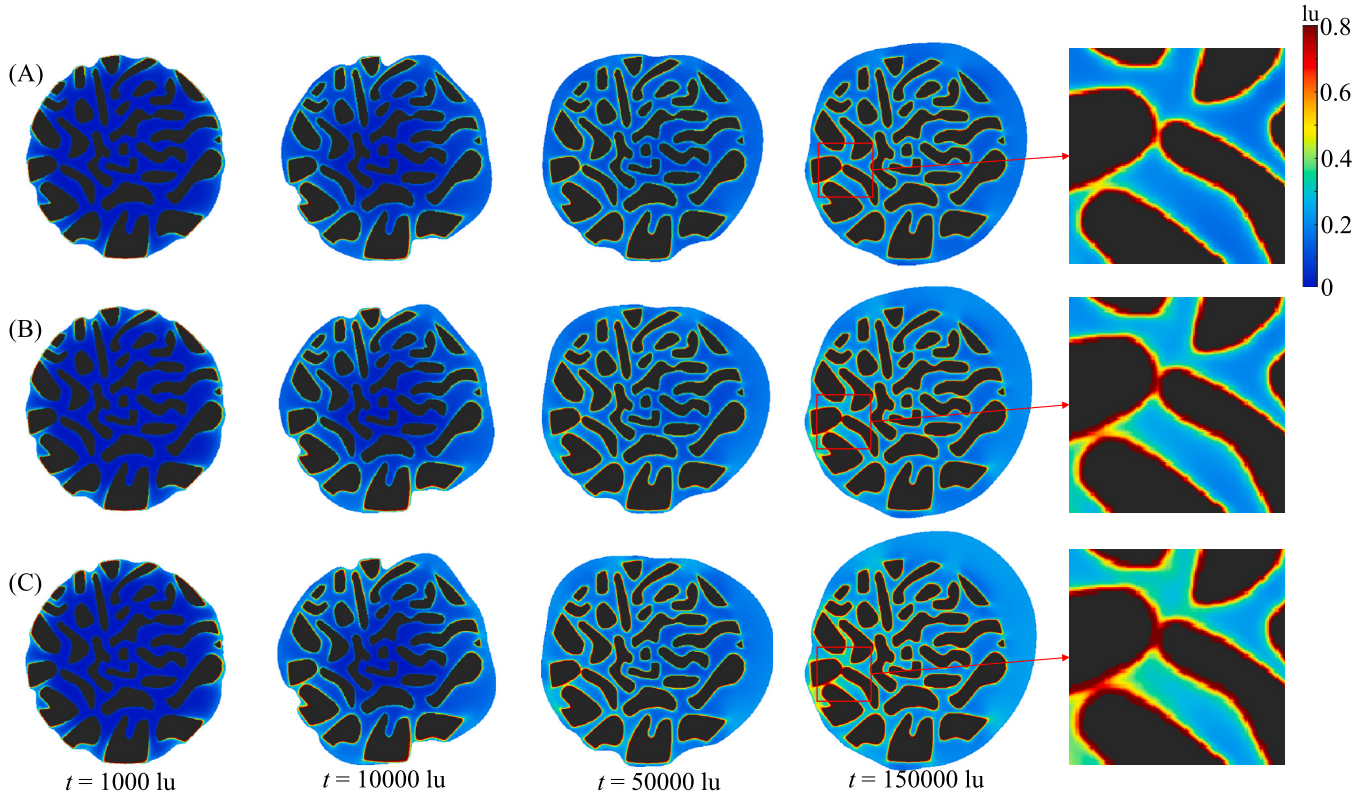

Fig. 14. The distribution of dissolved CO_2 concentration with different equilibrium dissolution concentrations. (A) $C_{eq}|_{c-co} = 0.2$ lu $= 3.63$ mol/L; (B) $C_{eq}|_{c-co} = 0.3$ lu $= 5.45$ mol/L; (C) $C_{eq}|_{c-co} = 0.4$ lu $= 7.26$ mol/L.

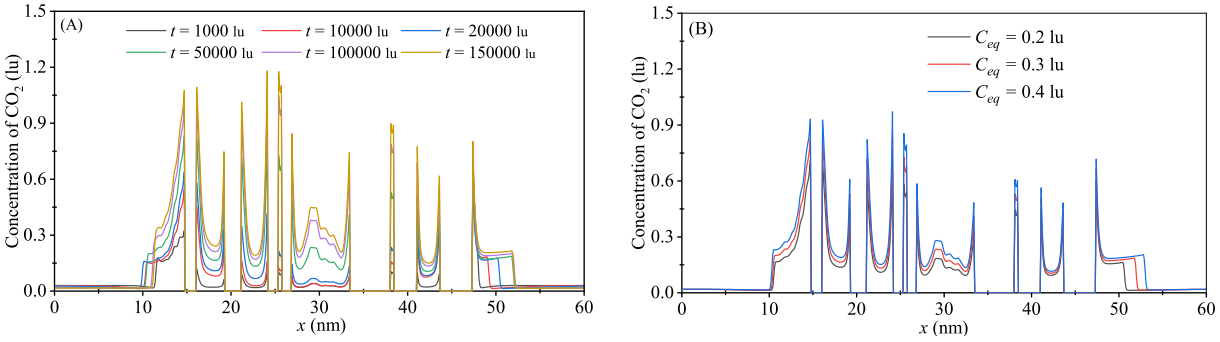

Fig. 15. The distribution curve of dissolved CO_2 concentration with different time and equilibrium dissolution concentrations. (A) Time with $C_{eq}|_{c-co} = 0.3$ lu = 5.45 mol/L; (B) equilibrium dissolution concentration with $t = 150{,}000$ lu.

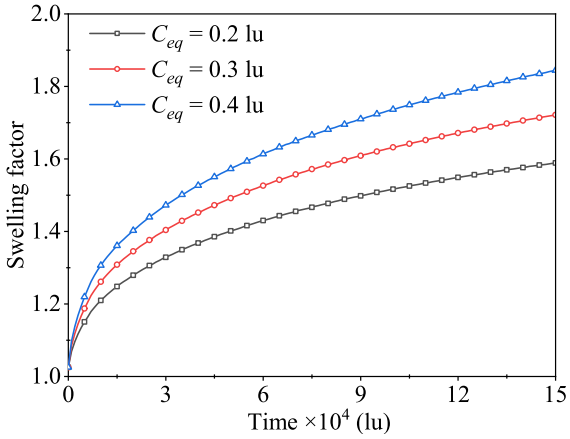

Fig. 16. Swelling factor of oil phase versus time.

porous media. The lattice size of the physical model is 600 × 600, and the corresponding physical size is 60 × 60 nm under the length scale of $L_0 = 1 \times 10^{-10}$ m. The upper, lower, left, and right boundaries are periodic boundary conditions, and the competitive adsorption boundaries of the oil and dissolved CO_2 phases on the solid surface are calculated by **Eq. (8)**. During the simulation, CO_2 gradually diffuses into the oil phase and is adsorbed on the solid surface, while the oil swells. When the equilibrium dissolution concentration equals to 0.3 lu = 5.45 mol/L, the immiscible CO_2 density distribution, dissolved CO_2 concentration distribution, and oil phase density distribution are shown in Fig. 13B-E.

Then the effects of equilibrium dissolution concentration on CO_2 diffusion, competitive adsorption, and oil swelling are studied and discussed. Fig. 14 illustrates the distribution of dissolved CO_2 concentration at different times and equilibrium dissolution concentrations. Fig. 15A shows the relationship between the distribution curve of dissolved CO_2 concentration along the red line in Fig. 13C with time. As CO_2 gradually diffuses into the oil phase through the oil-CO_2 interface region, the dissolved CO_2 is first adsorbed on the solid surface. Subsequently, it

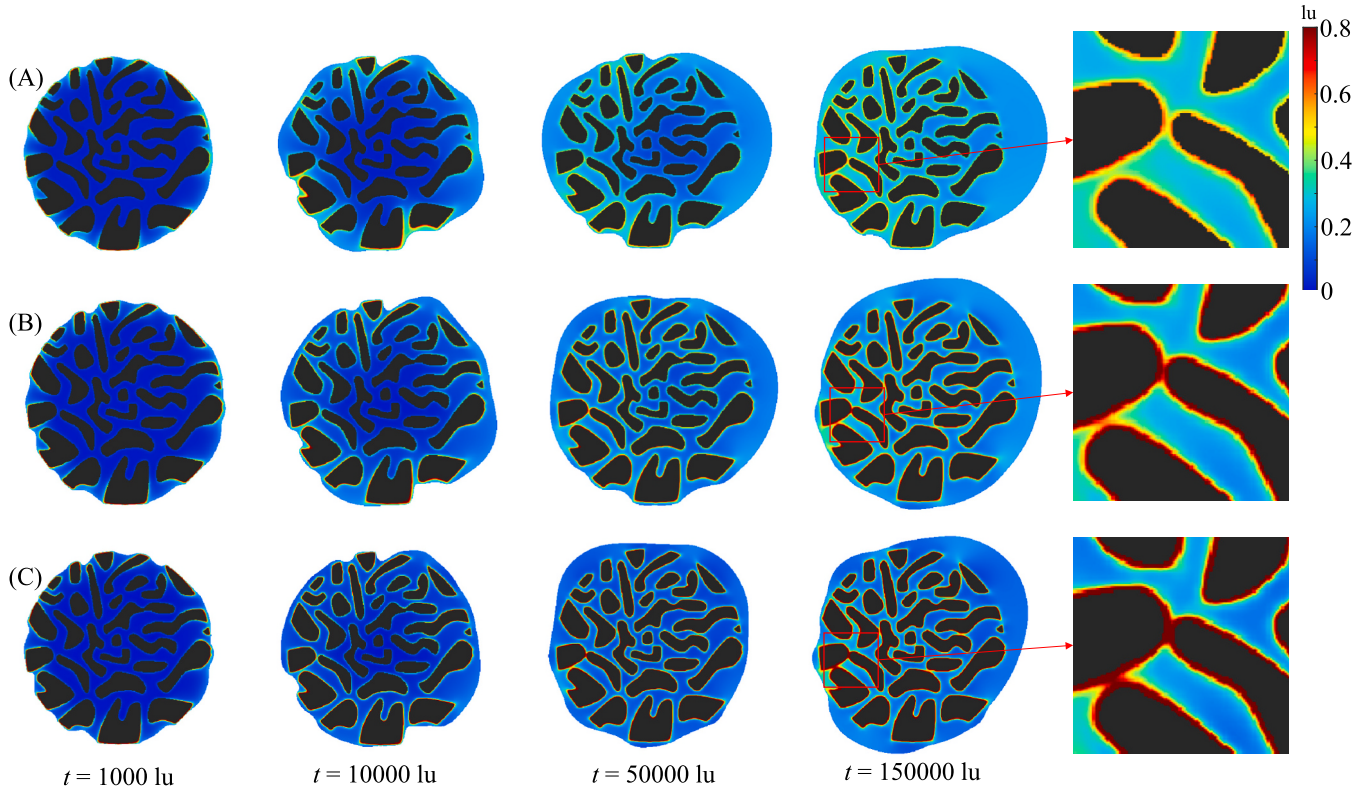

Fig. 17. The distribution of dissolved CO_2 concentration with different adsorption capacities. (A) $G_{c-o,ads} = -0.05$; (B) $G_{c-o,ads} = -0.1$; (C) $G_{c-o,ads} = -0.15$.

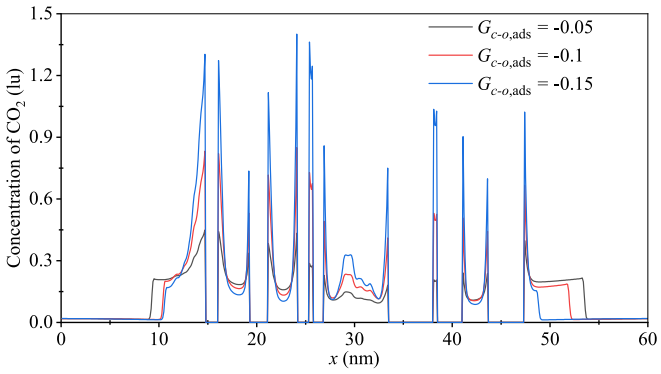

Fig. 18. The distribution curve of dissolved CO_2 concentration with different adsorption capacities, and t = 150,000 lu.

diffuses along the surface into the depths of the porous media [34], causing the oil phase to swell. As depicted in Fig. 14 and Fig. 15B, with the increase in equilibrium dissolution concentration, the concentration of dissolved CO_2 and the swelling volume of the oil increase. Then, a swelling factor is applied to evaluate oil swelling, defined as the ratio of the oil volume after swelling to that before diffusion. As shown in Fig. 16, the oil swelling factor gradually increases with increasing time and equilibrium dissolution concentration.

4.4. Effect of adsorption capacity

With the oil-dissolved CO_2 competitive adsorption parameter decreasing from −0.05 to −0.15, the adsorption capacity of dissolved CO_2 increases, and that of oil decreases. That is, the different competitive adsorption effects of oil-dissolved CO_2 on the solid surface are captured. With equilibrium dissolution concentration $C_{eq}|_{c-co}$ = 0.3 lu = 5.45 mol/L, the distribution of dissolved CO_2 concentration with different adsorption capacities ($G_{c-o,\text{ads}}$ = − 0.05, $G_{c-o,\text{ads}}$ = − 0.1, $G_{c-o,\text{ads}}$ = − 0.15) is illustrated in Fig. 17, and the distribution curve of dissolved CO_2 concentration with different adsorption capacities is presented in Fig. 18. With the increasing dissolved CO_2 adsorption capacity, the adsorption concentration of dissolved CO_2 in the near-wall region increases, while the concentration of dissolved CO_2 in the bulk phase decreases. The observation is consistent with the result before system equilibrium in section 4.2 **Diffusion and dissolution of CO_2 droplets**. An increase in dissolved CO_2 adsorption capacity enhances the diffusion rate of CO_2 in the oil phase, leading to a gradual increase in the total mass of dissolved CO_2 in the oil phase, as shown in Fig. 19A. Interestingly, the swelling factor of oil gradually decreases with increasing dissolved CO_2 adsorption capacity, as illustrated in Fig. 19B. The reason is that the dissolved CO_2 in the oil phase is mainly adsorbed on the solid surface due to the high adsorption capacity. As a result, the amount of dissolved CO_2 miscible with the bulk oil gradually decreases, leading to a decrease in the oil swelling factor.

5. Conclusions

In this paper, an improved MRT LBM coupled with multiphase multicomponent flow model and mass transfer model is established to model the behaviors of CO_2 diffusion through the oil-CO_2 immiscible interface, oil-dissolved CO_2 competitive adsorption on the mineral surfaces and oil swelling when the pressure is lower than MMP. The diffusion and oil swelling captured through the proposed model are successfully verified by the microfluidic experiment. Moreover, the model incorporates the effects of CO_2 diffusion and dissolution on the oil-CO_2-solid three-phase contact angle. Based on the proposed model, the diffusion/dissolution of CO_2 droplets and the process of CO_2 diffusion into the oil phase in nanoporous media, which causes competitive adsorption and oil swelling are simulated. The main findings are as follows:

As time increases, CO_2 gradually diffuses into the oil phase through the immiscible oil-CO_2 interface, and the volume of CO_2 droplets decreases. Additionally, the dissolved CO_2 concentration away from the solid gradually increases, approaching the equilibrium dissolution concentration, while the concentration in the near-wall region increases due to adsorption. With the increase in the equilibrium dissolution concentration, the dissolved CO_2 concentration in the oil phase increases. Meanwhile, the dissolution rate of CO_2 is accelerated, resulting in the increase of oil swelling volume and the dissolved CO_2 adsorption concentration. The effects of oil-dissolved CO_2 competitive adsorption on dissolved CO_2 diffusion and oil swelling in nanoporous media are completely different. Higher dissolved CO_2 adsorption capacity increases the mass of dissolved CO_2 diffusing into the oil phase. However, the oil swelling volume decreases due to the increase of dissolved CO_2 adsorption content near the solid surface.

CRediT authorship contribution statement

Han Wang: Writing – original draft, Validation, Supervision, Software, Methodology, Investigation, Funding acquisition, Formal analysis, Conceptualization. **Qinjun Kang:** Writing – review & editing, Validation, Methodology, Investigation, Formal analysis. **Wendong Wang:** Writing – review & editing, Methodology, Investigation, Formal analysis. **Wu He:** Software, Methodology, Formal analysis. **Yuxuan Xia:** Writing – original draft, Validation, Investigation, Data curation. **Jianchao Cai:** Writing – review & editing, Supervision, Methodology, Investigation, Conceptualization.

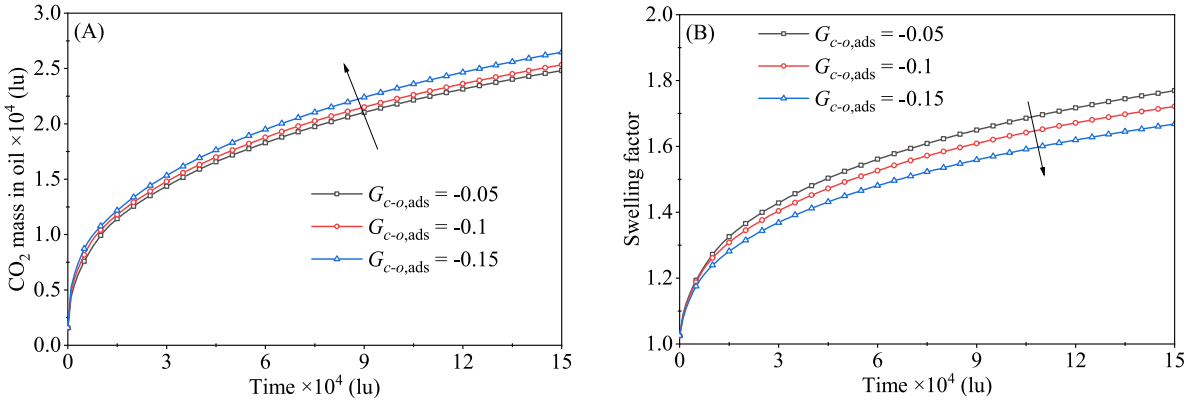

Fig. 19. The mass of dissolved CO_2 (A) and the swelling factor (B) under different adsorption capacities.

Declaration of competing interest

The authors declare that they have no known competing financial interests or personal relationships that could have appeared to influence the work reported in this paper.

Acknowledgment

This study was supported by the National Natural Science Foundation of China (52404048, 42172159), China Postdoctoral Science Foundation (2023M733872), Postdoctoral Fellowship Program of CPSF (GZB20230864).

Appendix A. Extended applications of the methodology

Combined with our previous work [17], our model enables the simulation of both miscible and immiscible diffusion mass transfer behaviors between shale oil and CO_2 across various pressures and temperatures. It reveals the process of enhancing shale oil recovery and realizing CO_2 geological storage through competitive adsorption on different mineral surfaces from a microscopic perspective. Meanwhile, our model facilitates the study of phase changes involving low-component hydrocarbon or dissolved CO_2 exsolution from the oil phase to form bubbles, which then results in the transformation from single-phase shale oil flow to two-phase oil-gas flow, allowing for an investigation into the influence mechanism of bubble exsolution on shale oil flow capacity. Moreover, the water phase in the pores, with varying wettability, can exhibit various forms such as droplets, water films, bridge plugs, clusters, etc., which obstructs the effective contact of oil and CO_2 through capillary force and interfacial force. This ultimately has a non-negligible effect on oil-CO_2 interaction [15,66-68]. Based on the approach presented in this paper, a three-phase three-component four-distribution MRT LBM could be developed to investigate the oil-water-CO_2 phase behaviors, considering the simultaneous diffusion and dissolution of CO_2 into the oil and water phase.

The proposed methodology mainly considers the physical processes of immiscible diffusion, oil swelling, and competitive adsorption. In practical applications, calibrating the relevant LB simulation parameters is necessary to ensure the simulation's accuracy. For immiscible diffusion and oil swelling behavior, although the LB simulation is two-dimensional, a two-dimensional microfluidic experimental method can be used for comparison and calibration. In section 3. **Model verification**, the successful calibration of microfluidic experimental results is discussed in detail. Moreover, the two-dimensional D2Q9 LBM can be easily extended to the three-dimensional D3Q19 LBM [69,70]. For oil-CO_2 competitive adsorption behavior, LB simulations cannot directly capture the real oil-CO_2-solid intermolecular interaction forces. Therefore, it is necessary to manually set the fluid-solid interaction parameters. The selection accuracy of this value is crucial for accurately applying the methodology can be accurately applied to enhance shale oil recovery and realize CO_2 geological storage. These intermolecular interaction forces can be captured accurately by molecular simulations, allowing for the determination of pore-scale fluid-solid interaction parameters by fitting the results from molecular simulations [15,17,71]. As shown in Fig. A1 [15], the fluid-solid interaction parameters were adjusted to match the miscible density distribution under real temperature and pressure obtained by molecular simulation. Therefore, based on the fitting microscopic parameters from both microfluidic experiments and molecular simulations, the proposed methodology can be effectively applied to shale oil recovery and CO_2 geological storage under real reservoir conditions.

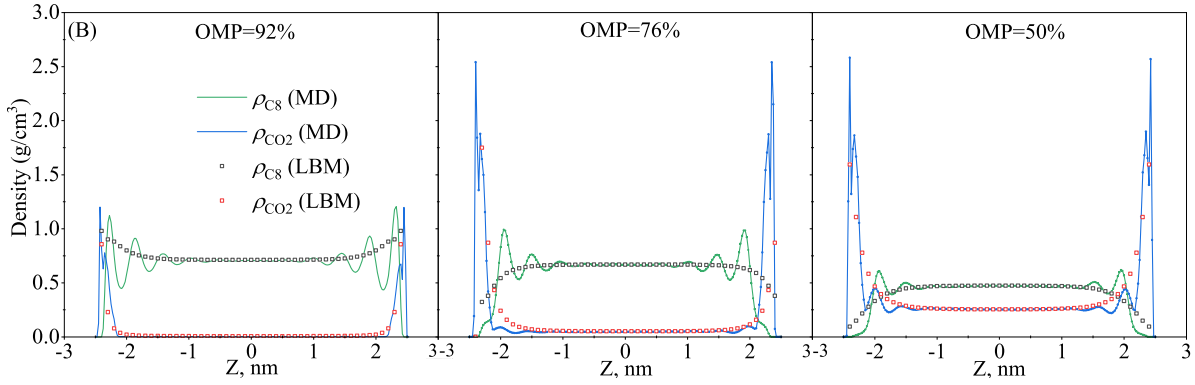

Fig. A1. Density distribution of nC8 and CO_2 from molecular dynamics (MD) and LB simulations [15]. OMP represents the oil mass percentage.

Data availability

Data will be made available on request.

References

[1] Y. Xu, Z. Lun, Z. Pan, H. Wang, X. Zhou, C. Zhao, D. Zhang, Occurrence space and state of shale oil: a review, J. Pet. Sci. Eng. 211 (2022) 110183.
[2] H. Wang, L. Chen, Z. Qu, Y. Yin, Q. Kang, B. Yu, W.-Q. Tao, Modeling of multi-scale transport phenomena in shale gas production—a critical review, Appl. Energy 262 (2020) 114575.
[3] W. Zhang, Q. Feng, S. Wang, J. Zhang, Z. Jin, T. Xia, X. Xing, P. Lv, Pore network modeling of oil and water transport in nanoporous shale with mixed wettability, J. Pet. Sci. Eng. 209 (2022) 109884.
[4] B. Pan, C.R. Clarkson, M. Atwa, C. Debuhr, A. Ghanizadeh, V.I. Birss, Wetting dynamics of nanoliter water droplets in nanoporous media, J. Colloid Interface Sci. 589 (2021) 411–423.
[5] F. Javadpour, H. Singh, A. Rabbani, M. Babaei, S. Enayati, Gas flow models of shale: a review, Energy Fuel. 35 (4) (2021) 2999–3010.
[6] J. Xu, S. Zhan, W. Wang, Y. Su, H. Wang, Molecular dynamics simulations of two-phase flow of n-alkanes with water in quartz nanopores, Chem. Eng. J. 430 (2022) 132800.
[7] J. Li, Z. Chen, K. Wu, T. Zhang, R. Zhang, J. Xu, R. Li, S. Qu, J. Shi, X. Li, Effect of water saturation on gas slippage in circular and angular pores, AIChE J. 64 (9) (2018) 3529–3541.
[8] T. Zhang, F. Javadpour, J. Li, Y. Zhao, L. Zhang, X. Li, Pore-scale perspective of gas/water two-phase flow in shale, SPE J. 26 (02) (2021) 828–846.
[9] H. Wang, W. Wang, Y. Su, Z. Jin, Lattice Boltzmann model for oil/water two-phase flow in nanoporous media considering heterogeneous viscosity, liquid/solid, and liquid/liquid slip, SPE J. 27 (06) (2022) 3508–3524.
[10] A.S. Chaudhary, C. Ehlig-Economides, R. Wattenbarger, Shale oil production performance from a stimulated reservoir volume, in: SPE Annual Technical Conference and Exhibition, OnePetro, 2011.
[11] X. Yang, J. Yan, C. Kangping, W. Shiming, The oil-gas two-phase flow model for shale reservoirs and its enlightenment to reservoir development, Acta Pet. Sin. 44 (2) (2023) 348–357.

[12] B. Jia, J.-S. Tsau, R. Barati, Role of molecular diffusion in heterogeneous, naturally fractured shale reservoirs during CO_2 huff-n-puff, J. Pet. Sci. Eng. 164 (2018) 31–42.
[13] Z. Peng, J. Sheng, Diffusion effect on shale oil recovery by CO_2 Huff-n-Puff, Energy Fuel. 37 (4) (2023) 2774–2790.
[14] J. Zou, W. Hu, Z. Lun, X. Zhou, C. Zhao, H. Wang, Z. Meng, P. Zhu, X. Tang, D. Zhang, Recovery of adsorbed and free oil in shale formations by CO_2 injection: an experimental study using 1D-and 2D-NMR, Energy Fuel. 38 (14) (2024) 12989–13001.
[15] H. Wang, J. Cai, Y. Su, Z. Jin, M. Zhang, W. Wang, G. Li, Pore-scale study on shale oil-CO_2-water miscibility, competitive adsorption, and multiphase flow behaviors, Langmuir 39 (34) (2023) 12226–12234.
[16] Z. Wu, Z. Sun, K. Shu, S. Jiang, Q. Gou, Z. Chen, Mechanism of shale oil displacement by CO_2 in nanopores: a molecular dynamics simulation study, Adv. Geo-Energy Res. 11 (2) (2024) 141–151.
[17] H. Wang, Y. Su, W. Wang, Z. Jin, H. Chen, CO_2-oil diffusion, adsorption and miscible flow in nanoporous media from pore-scale perspectives, Chem. Eng. J. 450 (2022) 137957.
[18] C. MacMinn, M. Szulczewski, R. Juanes, CO_2 migration in saline aquifers. Part 2. Capillary and solubility trapping, J. Fluid Mech. 688 (2011) 321–351.
[19] D. Bolster, The fluid mechanics of dissolution trapping in geologic storage of CO_2, J. Fluid Mech. 740 (2014) 1–4.
[20] H. Chen, X. Liu, C. Zhang, X. Tan, R. Yang, S. Yang, J. Yang, Effects of miscible degree and pore scale on seepage characteristics of unconventional reservoirs fluids due to supercritical CO_2 injection, Energy 239 (2022) 122287.
[21] M. Elturki, A. Imqam, Experimental investigation of asphaltene deposition and its impact on oil recovery in eagle ford shale during miscible and immiscible CO_2 huff-n-puff gas injection, Energy Fuel. 37 (4) (2023) 2993–3010.
[22] L. Yan, R. Niftaliyev, D. Voskov, R. Farajzadeh, Dynamics of salt precipitation at pore scale during CO_2 subsurface storage in saline aquifer, J. Colloid Interface Sci. 678 (2025) 419–430.
[23] R. Span, W. Wagner, A new equation of state for carbon dioxide covering the fluid region from the triple-point temperature to 1100 K at pressures up to 800 MPa, J. Phys. Chem. Ref. Data Monogr. 25 (6) (1996) 1509–1596.
[24] L. Li, Y. Zhang, J.J. Sheng, Effect of the injection pressure on enhancing oil recovery in shale cores during the CO_2 huff-n-puff process when it is above and below the minimum miscibility pressure, Energy Fuel. 31 (4) (2017) 3856–3867.
[25] C. Sambo, N. Liu, R. Shaibu, A.A. Ahmed, R.G. Hashish, A technical review of CO_2 for enhanced oil recovery in unconventional oil reservoirs, J. Pet. Sci. Eng. 221 (2022) 111185.
[26] P. Nguyen, J.W. Carey, H.S. Viswanathan, M. Porter, Effectiveness of supercritical-CO_2 and N_2 huff-and-puff methods of enhanced oil recovery in shale fracture networks using microfluidic experiments, Appl. Energy 230 (2018) 160–174.
[27] Y. Song, Z. Song, J. Guo, D. Feng, X. Chang, Phase behavior and miscibility of CO_2–hydrocarbon mixtures in shale nanopores, Ind. Eng. Chem. Res. 60 (14) (2021) 5300–5309.
[28] H. Gong, W. Lv, H. Zhang, M. Zhang, H. Sun, L. Xu, M. Dong, The influence and mechanism of alkyl block polyethers on the interfacial tension and minimum miscibility pressure of CO_2 and shale oil, Fuel 356 (2024) 129568.
[29] S. Kong, G. Feng, Y. Liu, K. Li, Potential of dimethyl ether as an additive in CO_2 for shale oil recovery, Fuel 296 (2021) 120643.
[30] H. Yu, H. Xu, W. Fu, X. Lu, Z. Chen, S. Qi, Y. Wang, W. Yang, J. Lu, Extraction of shale oil with supercritical CO_2: effects of number of fractures and injection pressure, Fuel 285 (2021) 118977.
[31] A. Grogan, V. Pinczewski, G.J. Ruskauff, F. Orr, Diffusion of CO_2 at reservoir conditions: models and measurements, SPE Reserv. Eng. 3 (1) (1988) 93–102.
[32] L. Li, Y. Su, Y. Hao, S. Zhan, Y. Lv, Q. Zhao, H. Wang, A comparative study of CO_2 and N_2 huff-n-puff EOR performance in shale oil production, J. Pet. Sci. Eng. 181 (2019) 106174.
[33] W. Zhang, Q. Feng, S. Wang, X. Xing, Z. Jin, CO_2-regulated octane flow in calcite nanopores from molecular perspectives, Fuel 286 (2021) 119299.
[34] D.Y. Moh, H. Zhang, S. Wang, X. Yin, R. Qiao, Soaking in CO_2 huff-n-puff: a single-nanopore scale study, Fuel 308 (2022) 122026.
[35] S. Afari, K. Ling, B. Sennaoui, D. Maxey, T. Oguntade, J. Porlles, Optimization of CO_2 huff-n-puff EOR in the Bakken formation using numerical simulation and response surface methodology, J. Pet. Sci. Eng. 215 (2022) 110552.
[36] W. Tang, J.J. Sheng, T. Jiang, Further discussion of CO_2 huff-n-puff mechanisms in tight oil reservoirs based on NMR monitored fluids spatial distributions, Pet. Sci. 20 (1) (2023) 350–361.
[37] X. Dong, W. Xu, H. Liu, Z. Chen, N. Lu, Molecular insight into the oil displacement mechanism of CO_2 flooding in the nanopores of shale oil reservoir, Pet. Sci. 20 (6) (2023) 3516–3529.
[38] T. Akai, M.J. Blunt, B. Bijeljic, Pore-scale numerical simulation of low salinity water flooding using the lattice Boltzmann method, J. Colloid Interface Sci. 566 (2020) 444–453.
[39] J. Zhao, F. Qin, Q. Kang, C. Qin, D. Derome, J. Carmeliet, A dynamic pore network model for imbibition simulation considering corner film flow, Water Resour. Res. 58 (7) (2022) e2022WR032332.
[40] W. Wang, Q. Xie, S. An, S. Bakhshian, Q. Kang, H. Wang, X. Xu, Y. Su, J. Cai, B. Yuan, Pore-scale simulation of multiphase flow and reactive transport processes involved in geologic carbon sequestration, Earth-Sci. Rev. 247 (2023) 104602.
[41] Z. Lanetc, A. Zhuravljov, Y. Jing, R.T. Armstrong, P. Mostaghimi, Coupling of transient matrix diffusion and pore network models for gas flow in coal, J. Nat. Gas Sci. Eng. 88 (2021) 103741.
[42] Q. Zhu, K. Wu, S. Guo, F. Peng, S. Zhang, L. Jiang, J. Li, D. Feng, Y. Zhang, Z. Chen, Pore-scale investigation of CO2-oil miscible flooding in tight reservoir, Appl. Energy 368 (2024) 123439.
[43] H. Zhao, Z. Ning, Q. Kang, L. Chen, T. Zhao, Relative permeability of two immiscible fluids flowing through porous media determined by lattice Boltzmann method, Int. Commun. Heat Mass Transf. 85 (2017) 53–61.
[44] X. Zhu, S. Wang, Q. Feng, L. Zhang, L. Chen, W. Tao, Pore-scale numerical prediction of three-phase relative permeability in porous media using the lattice Boltzmann method, Int. Commun. Heat Mass Transf. 126 (2021) 105403.
[45] H. Wang, J. Cai, Y. Su, Z. Jin, W. Wang, G. Li, Imbibition behaviors in shale nanoporous media from pore-scale perspectives, Capillarity 9 (2) (2023) 32–44.
[46] W. Wang, Q. Xie, H. Wang, Y. Su, S.R. Gomari, Pseudopotential-based multiple-relaxation-time lattice Boltzmann model for multicomponent and multiphase slip flow, Adv. Geo-Energy Res. 9 (2) (2023) 106–116.
[47] A.K. Gunstensen, D.H. Rothman, S. Zaleski, G. Zanetti, Lattice Boltzmann model of immiscible fluids, Phys. Rev. A 43 (8) (1991) 4320−4327.
[48] X. Shan, H. Chen, Lattice Boltzmann model for simulating flows with multiple phases and components, Phys. Rev. E 47 (3) (1993) 1815−1819.
[49] M.R. Swift, W. Osborn, J. Yeomans, Lattice Boltzmann simulation of nonideal fluids, Phys. Rev. Lett. 75 (5) (1995) 830−833.
[50] L. Chen, Q. Kang, Y. Mu, Y.-L. He, W.-Q. Tao, A critical review of the pseudopotential multiphase lattice Boltzmann model: methods and applications, Int. J. Heat Mass Transf. 76 (2014) 210–236.
[51] Q. Li, Q. Kang, M.M. Francois, Y. He, K. Luo, Lattice Boltzmann modeling of boiling heat transfer: the boiling curve and the effects of wettability, Int. J. Heat Mass Transf. 85 (2015) 787–796.
[52] P. Lallemand, L.S. Luo, Theory of the lattice Boltzmann method: dispersion, dissipation, isotropy, Galilean invariance, and stability, Phys. Rev. E 61 (6) (2000) 6546−6562.
[53] T. Lei, K.H. Luo, F.E.H. Pérez, G. Wang, Z. Wang, J.R. Cano, H.G. Im, Study of CO_2 desublimation during cryogenic carbon capture using the lattice Boltzmann method, J. Fluid Mech. 964 (2023) A1.
[54] J. Wu, Y. Gan, Z. Shi, P. Huang, L. Shen, Pore-scale lattice Boltzmann simulation of CO_2-CH_4 displacement in shale matrix, Energy 278 (2023) 127991.
[55] L. Chen, M. Wang, Q. Kang, W. Tao, Pore scale study of multiphase multicomponent reactive transport during CO_2 dissolution trapping, Adv. Water Resour. 116 (2018) 208–218.
[56] J. Yang, Q. Xu, Z. Liu, L. Shi, Pore-scale study of the multiphase methane hydrate dissociation dynamics and mechanisms in the sediment, Chem. Eng. J. 430 (2022) 132786.
[57] Q. Xie, W. Wang, Y. Su, H. Wang, Z. Zhang, W. Yan, Pore-scale study of calcite dissolution during CO_2-saturated brine injection for sequestration in carbonate aquifers, Gas Sci. Eng. 114 (2023) 204978.
[58] N.S. Martys, H. Chen, Simulation of multicomponent fluids in complex three-dimensional geometries by the lattice Boltzmann method, Phys. Rev. E 53 (1) (1996) 743−750.
[59] R. Benzi, L. Biferale, M. Sbragaglia, S. Succi, F. Toschi, Mesoscopic modeling of a two-phase flow in the presence of boundaries: the contact angle, Phys. Rev. E 74 (2) (2006) 021509.
[60] S. Sullivan, F. Sani, M. Johns, L. Gladden, Simulation of packed bed reactors using lattice Boltzmann methods, Chem. Eng. Sci. 60 (12) (2005) 3405–3418.
[61] Q. Li, K. Luo, X. Li, Lattice Boltzmann modeling of multiphase flows at large density ratio with an improved pseudopotential model, Phys. Rev. E 87 (5) (2013) 053301.
[62] L. Chen, Q. Kang, Q. Tang, B.A. Robinson, Y. He, W. Tao, Pore-scale simulation of multicomponent multiphase reactive transport with dissolution and precipitation, Int. J. Heat Mass Transf. 85 (2015) 935–949.
[63] D. Janiga, R. Czarnota, E. Kuk, J. Stopa, P. Wojnarowski, Measurement of oil-CO_2 diffusion coefficient using pulse-echo method for pressure-volume decay approach under reservoir conditions, J. Pet. Sci. Eng. 185 (2020) 106636.
[64] J.A. Von Fraunhofer, Adhesion and cohesion, Int. J. Dentist. 2012 (1) (2012) 951324.
[65] X. Zhang, L. Li, Y. Su, Q. Da, J. Fu, R. Wang, F. Chen, Microfluidic investigation on asphaltene interfaces attempts to carbon sequestration and leakage: oil-CO2 phase interaction characteristics at ultrahigh temperature and pressure, Appl. Energy 348 (2023) 121518.
[66] Y. Luan, X. Dou, Y. Zhou, P. Hao, B. Liu, J. Liu, Effect of the water film rupture on the oil displacement by supercritical CO2 in the nanopore: molecular dynamics simulations, Energy Fuel. 36 (8) (2022) 4348–4357.
[67] B. Liu, W. Liu, Z. Pan, L. Yu, Z. Xie, G. Lv, P. Zhao, D. Chen, W. Fang, Supercritical CO_2 breaking through a water bridge and enhancing shale oil recovery: a molecular dynamics simulation study, Energy Fuel. 36 (14) (2022) 7558–7568.
[68] X. Qin, H. Wang, Y. Xia, X. Jiao, G. Wang, J. Cai, Pore-scale investigation of water-CO_2-oil flow in shale fractures for enhanced displacement efficiency and CO_2 sequestration, Eng. Geology 348 (2025) 107969.
[69] H. Wang, M. Zhang, X. Xia, Z. Tian, X. Qin, J. Cai, Lattice Boltzmann prediction of CO_2 and CH_4 competitive adsorption in shale porous media accelerated by machine learning for CO_2 sequestration and enhanced CH_4 recovery, Appl. Energy 370 (2024) 123638.
[70] X. Zhou, J. Sheng, Z. Ye, Evaluation of immiscible two-phase quasi-static displacement flow in rough fractures using LBM simulation: effects of roughness and wettability, Capillarity 11 (2) (2024) 41–52.
[71] H. Wang, J. Huang, S. Zhan, M. Zhang, J. Cai, Study on CO_2 and CH_4 competitive adsorption in shale organic and clay porous media from molecular- to pore-scale simulation, SPE J. 29 (6) (2024) 3265–3276.